Environment Canada
Environnement Canada

Environmental Protection Service
Service de la protection de l'environnement

Microwave Systems for Detecting Oil Slicks in Ice-infested Waters: Phases II and III

Economic and Technical Review
Report EPS 3-EC-80-3

Environmental Impact Control Directorate
September 1980

ENVIRONMENTAL PROTECTION SERVICE REPORT SERIES

Economic and Technical Review Reports relate to state-of-the-art reviews, library surveys, industrial inventories, and their associated recommendations where no experimental work is involved. These reports will either be undertaken by an outside agency or by the staff of the Environmental Protection Service.

Other categories in the EPS series include such groups as Regulations, Codes, and Protocols; Policy and Planning; Technology Development; Surveillance; Training Manuals; Briefs and Submissions to Public Inquiries; and, Environmental Impact and Assessment.

Inquiries pertaining to Environmental Protection Service Reports should be directed to the Environmental Protection Service, Department of the Environment, Ottawa, Ontario, Canada, K1A 1C8.

Minister of Supply and Services Canada 1980
Cat. No. En 46-3/80-3
ISBN 0-662-50930-7

MICROWAVE SYSTEMS FOR DETECTING OIL SLICKS IN ICE-INFESTED WATERS: PHASES II AND III

by

C-CORE
Centre for Cold Ocean Resources
Engineering
Memorial University of Nfld.
St. John's, Nfld.

for the

Environmental Emergency Branch
Environmental Impact Control Directorate
Environmental Protection Service
Environment Canada

EPS 3-EC-80-3
September 1980

REVIEW NOTICE

This report has been reviewed by the Environmental Impact Control Directorate, Environmental Protection Service, and approved for publication. Approval does not necessarily infer that the content reflects the views and policies of the Environmental Protection Service. Mention of trade names or commercial products does not consitute endorsement for use.

ABSTRACT

Two ice regimes, one corresponding to waves in ice and the other depicting an iceberg, were selected for analysis of the potential of microwave systems for detecting oil in an ice regime. The results obtained from the manual and digital analysis of 4-channel SAR imagery of these regions are presented and discussed in terms of their relevance to the potential of detecting oil pollution in the ice environment through SAR. The digital analysis consisted of generating histograms, statistics, clutter to noise ratios and grey-tone reproduction. The available digital data corresponded to 8-bit digitization of the square-root of the video.

The results indicate that squaring of the available data reproduces the original data more faithfully than the unsquared data. For grey-tone reproduction equal density quantization is more desirable than the equal interval quantization. It appears that the likelihood of detecting oil pollution in the ice environment through SAR can be improved and false alarm risk decreased by collecting SAR data with appropriate gain settings so that return from open water areas falls in the middle of the dynamic range of the system. The resulting digital data can be enhanced by using simple techniques, and reproduced through inexpensive graphic recorders.

RÉSUMÉ

Deux régimes de glaces flottantes, l'un correspondant à des ondes réfléchies par la glace et l'autre par un iceberg, servent de cadre à l'analyse de la détectabilité des hydrocarbures en milieu de glaces flottantes par des systèmes micro-ondes. Les résultats des analyses manuelle et numérique des images de ces zones, captées dans 4 voies par radar à ouverture synthétique (SAR), sont présentés et examinés en fonction de leur pertinence dans la détection des hydrocarbures en milieu de glaces flottantes par ce type de radar. Les opérations numériques comportent l'élaboration d'histogrammes, l'établissement de statistiques et de rapports parasites-bruit et la reproduction d'images dans la gamme de gris. Les données numériques présentées ont été obtenues par digitalisation sur 8 bits de la racine carrée des valeurs du signal vidéo.

Les résultats indiquent que les données originales peuvent être reproduites plus fidèlement par les données numériques élevées au carré. La quantification en densités égales se révèle une meilleure méthode que la quantification en intervalles égaux pour la reproduction d'images dans la gamme de gris. Il semble aussi que la détection des hydrocarbures en milieu de glaces flottantes peut être améliorée et que les risques de fausses alertes peuvent être diminués par des réglages de gain appropriés au stade de la collecte des données. Ainsi, les échos provenant des zones d'eau libre pourront se trouver au milieu de la gamme dynamique du système. Les données numériques obtenues peuvent être améliorées par des méthodes simples et reproduites à l'aide d'enregistreurs graphiques peu coûteux.

FOREWORD

This report outlines the results of a study concerning the detection of oil slicks in an ice environment using microwave systems. The work covered by this report was executed by C-CORE with Dr. R.A. O'Neil of the Canada Centre for Remote Sensing (CCRS) as scientific authority. The report was supported under contract No. EOSQ77-00154 by CCRS as part of the Arctic Marine Oil Spill Program (AMOP), sponsored by the Research and Development Division, Environmental Emergencies Branch, Environmental Protection Service, Environment Canada.

TABLE OF CONTENTS

LIST OF FIGURES

LIST OF TABLES

CONCLUSIONS AND RECOMMENDATIONS

The results obtained from analyzing a limited amount of digital radar data are inconclusive in terms of preference of one channel over the other, for potential in detecting oil in the ice environment. The computed values of signal to noise ratio show that X-band channels provide more contrast between other regions. In general, it appears cross-polarized channels provide more contrast than the like-polarized channels.

Only simple statistics were computed from the radar digital data for regions of interest. The textural parameters are likely to provide additional information. The task is to devise means for increasing contrast between potential polluted and unpolluted regions. The equal density quantization and the use of simple inexpensive graphic recorders for grey-tone display provide a means to increase the tonal and textural contrast. It is only through the analysis of SAR data over actual oil spilled in the ice environment that the utility of SAR can be assessed. By operating SAR with proper gain adjustments and processing the resulting data as suggested the possibility of detecting oil is likely to be improved.

1 INTRODUCTION

A study was undertaken to ascertain possibilities and limitations associated with the use of active and passive microwave systems for oil pollution surveillance in the ice environment. The study was conducted for the Canada Centre for Remote Sensing (CCRS), under the Arctic Marine Oil Pollution (AMOP) Program of Environmental Protection Service (EPS). Phase I of the three phase study, contained an assessment and analysis of the known microwave emission and scattering properties of sea ice, oil on water, and the ocean surface. The available information on the electrical properties of oil and the behaviour of oil spilled in the ice environment were also considered. A selected annotated bibliography of the pertinent literature was prepared. The results of the investigation presented in the Phase I report (C-CORE, 1978) show that the available information only warrants a qualitative assessment of the potential performance of active and passive systems in detecting and monitoring oil pollution in the ice environment. It appears the presence of oil in the ice environment is likely to be detected through identification of indirect subtle clues, i.e., changes in texture and tone such as those produced by increased melting of oil-covered areas in comparison with oil-free areas. As the changes, if any, produced in tone and texture on the images (both radar and radiometer) due to the presence of oil are expected to be subtle, it was felt desirable to begin investigating the variability of signatures in the ice environment. The investigation should provide information on ways of processing and enhancing the radar data and of reducing the false alarm risk. The contrast between polluted and unpolluted regions must be identified and ways devised to enhance the contrast and reduce false alarm risk. To accomplish this task, it was decided to utilize 4-channel synthetic aperture (SAR) imagery of sea ice (Worsfold et al, 1977). From this large set of images, about thirty regions were recommended under Phase II of the contract for further consideration.

The criteria for selecting regions under Phase II were: quality of imagery on all four channels; variability of sea ice types and conditions; and the utility to the AMOP project. The relevance of the regions to the AMOP project was deduced from considerations of the type of conditions which may likely be present or occur in the region of an oil spill. The likelihood of oil spill detection is influenced by, among other things, ice concentration, and the type and conditions of ice (Parashar et al, 1978a). The areas which are likely to be mistaken for an oil spill are the regions of ice and open water which give a relatively black tone (low return) on the radar image.

Two regions were finally selected for further study under Phase III, because of time and financial constraints. One of the regions contained an iceberg surrounded by various types of thin ice, and radar data were available in digital format on the computer compatible tape (CCT). The other region, for which no digital data were available, contained flexured waves in ice and possibly some areas of open water. This report is concerned with the manual and digital analysis of these two data sets, and a discussion of the results obtained. A brief discussion of the ice conditions off the east coast of Labrador and Newfoundland, with examples from SAR '77 data, is also presented.

2 AVAILABLE DATA

2.1 Ice Conditions in Labrador Sea

The ice conditions off the east coast of Labrador and Newfoundland are very dynamic and vary from year to year. The main factors which influence ice conditions are air temperature, wind, sea state, and currents. The limited information available about this region has been compiled in the preparation of an oil spill scenario for the Labrador Sea under AMOP (LeDrew and Gustajtis, 1978). Ice found off the coast of Labrador consists of locally formed fast ice and open sea pack ice, ice from the Arctic Basin, and icebergs. The locally formed ice does not survive the summer's melt and whatever second-year and multi-year ice is found has apparently drifted south from the Arctic.

The available information based on field measurements made in conjunction with Project SAR '77 (Winsor and LeDrew, 1978) indicates that the process of ice formation in the Labrador Sea goes through a continual cycle of thorough break-up and reconsolidation. As a result, the prevailing ice conditions include extensive floes of consolidated cakes separated by a network of leads, loosely agglomerated individual cakes broken from larger floes due to wave action, or solid ice cover resulting from lateral compression of the cakes. The well-rounded cakes have raised edges, and vary in size from 2 to 9 m in diameter. The typical thickness for the Labrador Sea pack ice is about 2 m, with ridges having greater thickness.

2.2 SAR Data

The SAR data presented and discussed in the report were obtained using Environmental Research Institute of Michigan (ERIM) system operating simultaneously in the X(3 cm wavelength) and L(25 cm), bands with capability of transmitting either horizontal or vertical polarizations and receiving both like- and cross-polarizations. The areas imaged and the type of data collected during Project SAR'77 undertaken in February and March 1977 are presented in Project SAR '77, Field Data Report E1 (Larson et al, 1977).

The obtained imagery was processed to a spatial resolution of 3m x 3m and 6m x 6m for X- and L-band data respectively. The imagery presented here is in the slant range mode, with a swath width of about 5200 m. The imagery was obtained from an altitude of about 3,000 m using antenna depression angle of 30^{o}. The processing of the data from signal film into image film was done by ERIM through their Precision Optical

Processor. The digitization of the radar data from signal film onto digital magnetic tapes was also done by ERIM through their hybrid image processing facility. The areas digitized and the procedure employed are described by Rawson et al, (1978). Prior to 8-bit digitization, square roots of the intensity values were taken so larger dynamic range of intensity values could be handled. The sampling rate was such as to provide a pixel, (the smallest unit of definition; picture element, which can usually be defined by the size of image area it represents) size of 1.5 x 1.5 m. The resulting digitized values, each ranging from 0 to 255, were stored on 9-track, 800 bpi, magnetic tapes.

2.3 General Radar Ice Interpretation

The 4-channel SAR imagery obtained under Project SAR '77 and presented in Figures 1 through 4, illustrate the transition zone off Hopedale, Labrador. The flight and antenna look directions are marked by the arrows. This region was labelled AMOP 6 for Phase II and consists of non-overlapping imagery of passes 8, 9, 10, and 11 flown on February 25, 1977 (antenna depression angle 30^{o}). This section of the imagery covers an area of shear zone which contains the ice edge in the central portion. An area of dynamic pack ice lies seaward to the east of the edge while an area of transitional, heavily ridged sea ice having ridge heights in the 2 m range lies to the west of the edge. Shear lines and discontinuities are visible in this region. Striations are evident in the radar return and may define an ice edge which existed in the past. The ice cover seaward of the ice edge appears to be all new ice followed by a section of relatively older ice as more clearly depicted on the L-band than on the X-band imagery. The areas appearing relatively black on the X-band images are usually termed "open water" areas. But inspection of the L-band imagery of these areas shows some tone and texture, suggesting the presence of very thin ice not evident on the X-band image. Features in the shear zone shoreward from the ice edge are more well defined on the X-band imagery than the L-band.

In general, relative contrast between features appears to be produced more on the HV imagery than on HH. The possible role of volume scattering in producing relatively more contrast between new and older ice forms and its dependence on porosity is discussed by Parashar et al, (1978b). The X-band imagery tends to show fine features of ice conditions in fast ice whereas L-band shows gross variations. The ability of 4-channels in providing more information than one channel alone is evident. However, the contributing factors which are responsible for the observed differences in channels are not known.

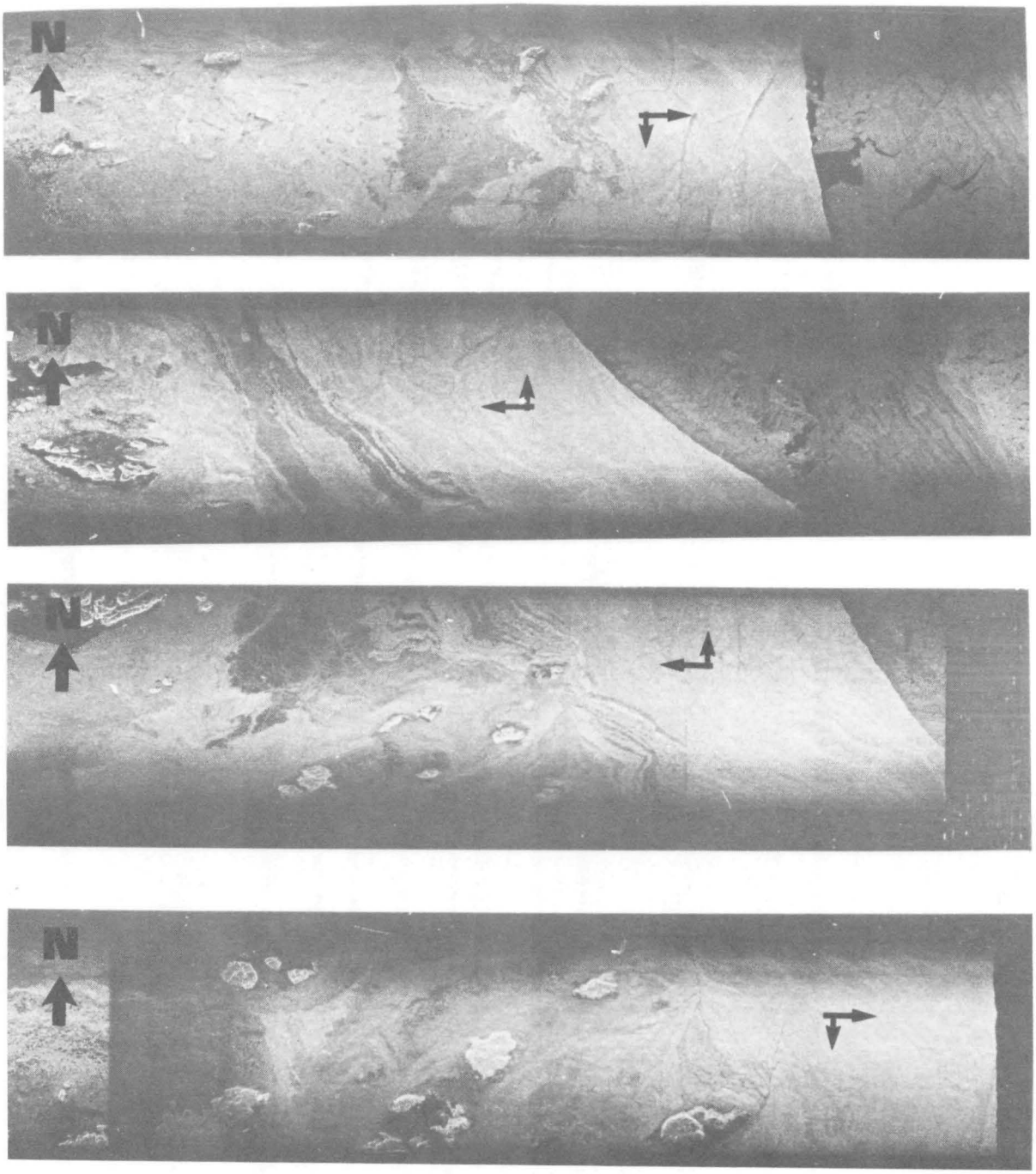

FIGURE 1 SAR IMAGERY, REGION AMOP 6; PASS 8, 9, 10, 11
X-BAND HV, FEBRUARY 25, 1977.
(Location: Lat. 55°30'N, Long. 59°35'W near Hopedale, Labrador)

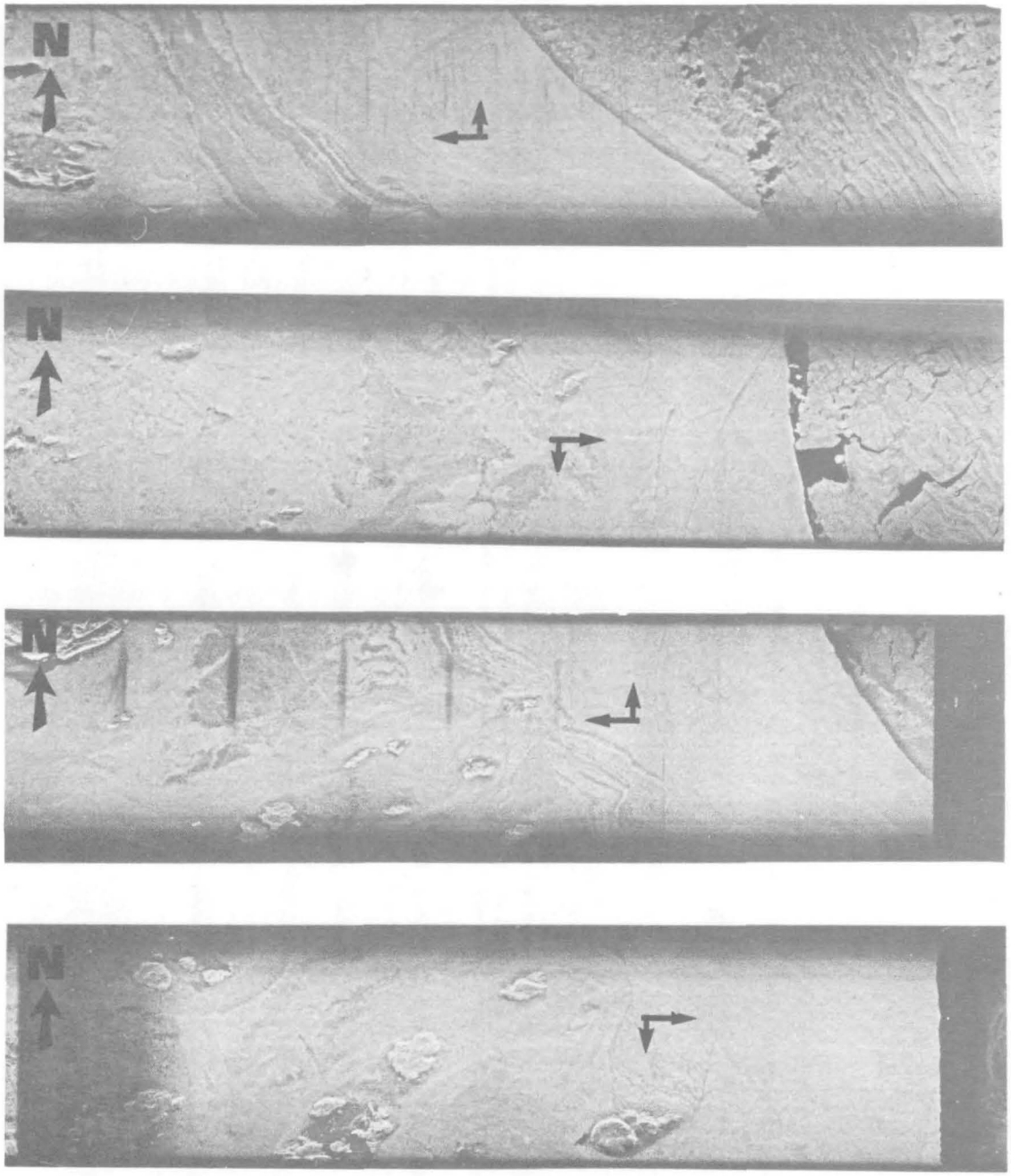

FIGURE 2 SAR IMAGERY, REGION AMOP 6; PASS 8, 9, 10, 11
X-BAND HH, FEBRUARY 25, 1977.
(Location: Lat. 55°30'N, Long. 59°35'W near Hopedale, Labrador)

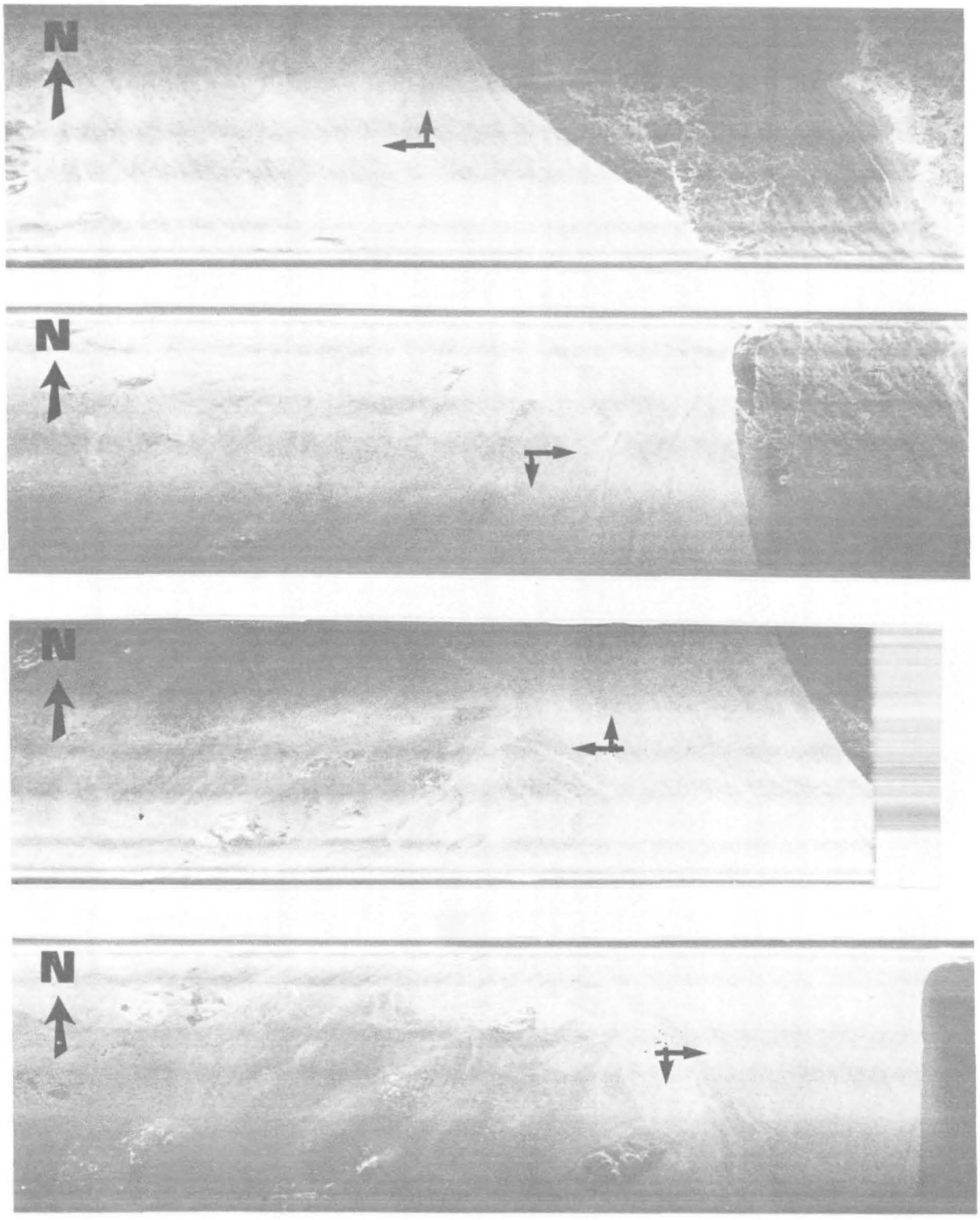

FIGURE 3 SAR IMAGERY, REGION AMOP 6; PASS 8, 9, 10, 11
L-BAND HV, FEBRUARY 25, 1977.
(Location: Lat. 55°35'N, Long. 59°35'W near Hopedale, Labrador)

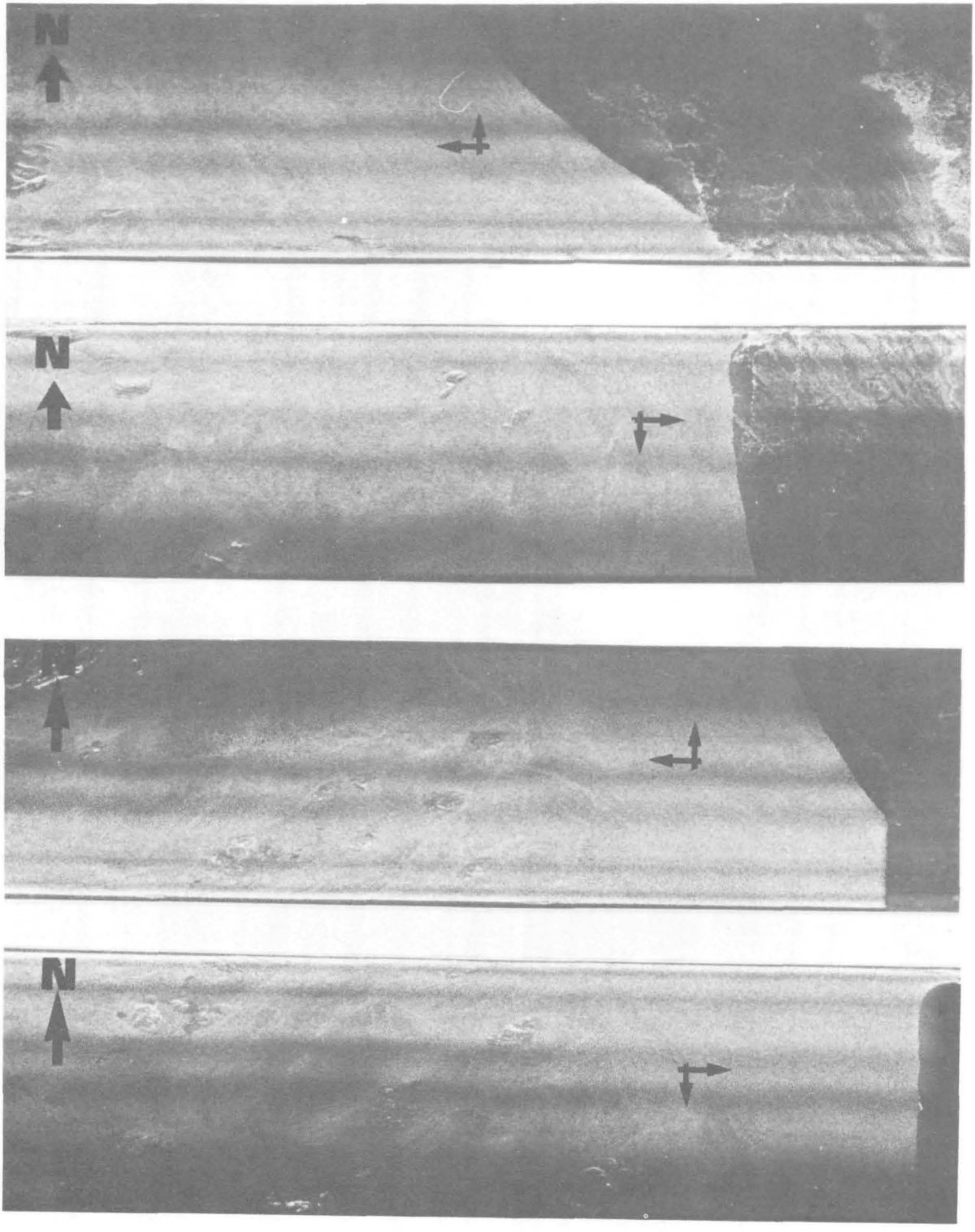

FIGURE 4 SAR IMAGERY, REGION AMOP 6; PASS 8, 9, 10, 11
L-BAND HH, FEBRUARY 25, 1977.
(Location Lat. 55°30'N, Long. 59°35'W near Hopedale, Labrador)

Results similar to those previously presented are obtained from the interpretation of imagery of region labelled AMOP 16, (see Figures 5 and 6). The passes 1 and 2 shown in Figures 5 and 6 respectively were imaged with reciprocal headings and a slight overlap in the obtained imagery. The region on pass 1 extends northeast of Holton Island out over the shear zone. The contrast between X-band and L-band imagery is particularly noticeable with L-band showing ridges more sharply and X-band giving more detail in the fast ice areas. Different types of ice conditions are depicted in the region labelled AMOP 19 from pass 7, (see Figure 7). The similarity between the returns recorded on both X-band and L-band channels is striking. Floes ranging in size from large pans down to small are well defined. In general, there appears to be more contrast between features on the HV imagery than on the HH.

2.4 Theoretical Considerations

The nature of radar scattering from sea ice has yet to be fully understood. Some parameters of sea ice such as brine volume, temperature, surface roughness, and porosity have been identified, but information is lacking on how these parameters interact to produce observed changes in radar scattering. The skin depth for sea ice with a salinity of about $2^{o}/oo$ has been found to be in the order of one wavelength at $-10^{o}C$ and decreases with increasing frequency, temperature and salinity. Although no "ground truth" information is available for the ice depicted in the Figures 1-4, nearby 40 cm thick fast ice had a salinity of about $6^{o}/oo$, and the air temperature was about $-12^{o}C$. The radar scattering is expected to be influenced by the characteristics of the top few centimetres at X-band and about 20 cm at L-band. A surface having variations in height of more than a few millimetres is considered rough at X-band and a few centimetres at L-band. A surface which appears rough at X-band may appear smooth at L-band. In addition to variations in the vertical dimensions, the corresponding horizontal scale is important too.

The real part of complex permittivity of pure ice is about 3.2. The corresponding value for sea ice increases with increasing salinity and may be as high as 6 or more. The value of dielectric constant of sea ice decreases with temperature and appears to be independent of frequency in the range of interest.

The computed value of radar scattering coefficient, σ^{o}, at 13.3GHz, HH polarization, presented by Parashar (1974) indicates that a decrease in surface salinity of about $3^{o}/oo$, decreases the σ^{o} value for incidence angles of 20 to 60 degrees for less than 1 dB. By doubling the surface roughness value, an increase of 6 dB in the value of σ^{o} is obtained. It appears, therefore, that radar scattering is more sensitive to changes in

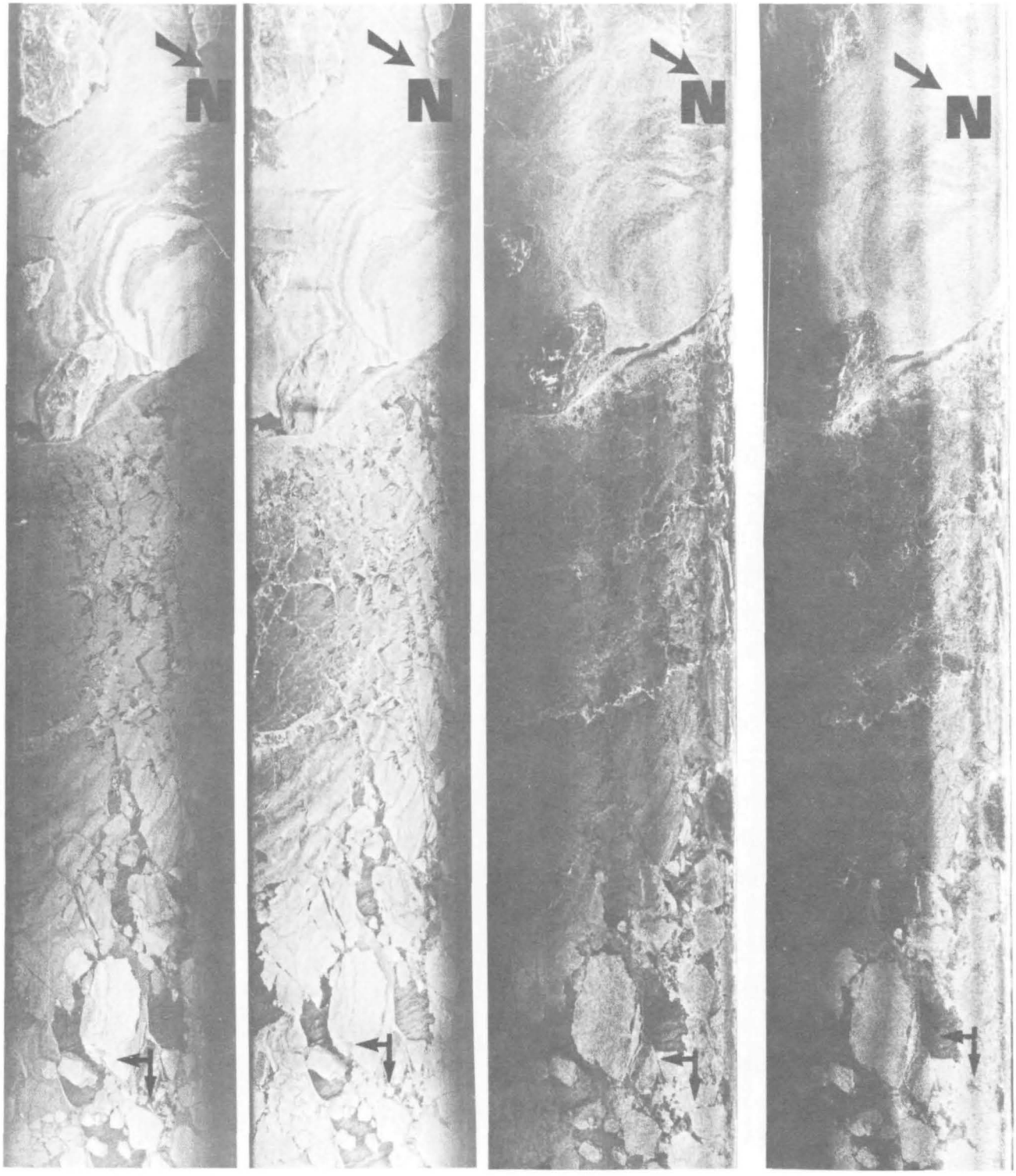

FIGURE 5 SAR IMAGERY, REGION AMOP 16, PASS 1;
X-BAND HV AND HH, L-BAND HV AND HH, FEBRUARY 24, 1977.
(Location: NE of Holton Island, Labrador; Lat. 54° 37.5'N. Long. 57° 17'W)

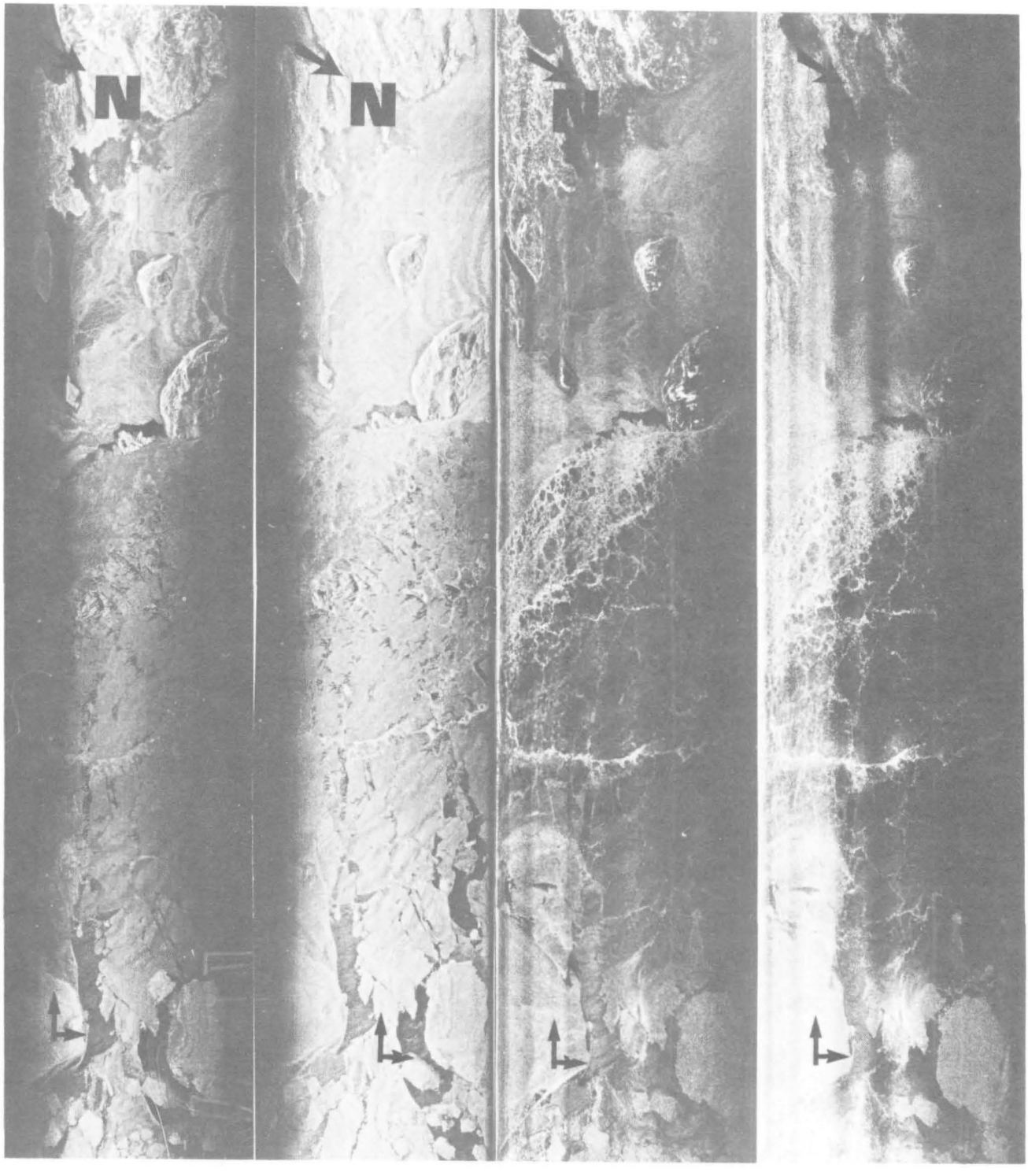

X-HV X-HH L-HV L-HH

FIGURE 6 SAR IMAGERY, REGION AMOP 16, PASS 2;
X-BAND HV AND HH, L-BAND HV AND HH, FEBRUARY 24, 1977.
(Location: NE of Holton Island, Labrador; Lat. 54°37.5'N, Long. 57°17'W)

FIGURE 7 SAR IMAGERY, REGION AMOP 19, PASS 7;
X-BAND HV AND HH, L-BAND HV AND HH, FEBRUARY 25, 1977.
(Location: Lat. 54°35'N, Long. 55°30'W)

surface roughness than the variations in salinity and temperature. It is difficult to quantitatively assess the contributing parameters responsible for observed changes in the radar scattering within one channel, and between channels, because of lack of information and an associated scattering model.

3 RESULTS

The radar imagery of the two regions selected for further study under Phase III are shown in Figures 8 and 9. The region labelled AMOP 18 depicting waves propagating ice is presented in Figure 8. No digital data are available for the region. Another region labelled Iceberg 1 is shown in Figure 9. The area for which digital data are available is shown by the marked rectangle on Figure 9.

3.1 Region 1 - AMOP 18

The striking feature of the imagery presented in Figure 8 is the lack of waves present in the dark portions of the imagery. These relatively dark toned areas may correspond to open water or very thin new ice. The presence of some wave pattern in these areas is more evident on the L-band than on the X-band imagery and correspondingly more on the HV channel than on HH.

The actual mechanism responsible for imaging waves by SAR is not known. The SAR imaging of ocean waves is generally attributed to the presence of capillary waves in open ocean whose brightness on the final image is determined by swell, slope, capillary dynamics, doppler and focus modulations. The four theoretical models proposed by Elachi and Brown (1977) to explain the method which enables ocean swell to be imaged by SAR are; tilt modulation, roughness modulation, orbital velocity, and parametric effects. The velocity effects of wave motions on SAR are discussed in terms of the swell phase velocity by Shuchman et al, 1977. No single explanation has been found to be entirely suitable, and examples can be found which support or contradict one or more of the above models.

In examining these models further, Raney and Lowry (1978) have tried to show that for uncrested waves (non-cycloidel, such as long swells modulated by capillaries) the appropriate model is based on orbital motion of the capillaries with an explicit inclusion of the vertical component of the underlying gravity wave motion. The most suitable model for breaking or crested waves is based on the phase velocity of the gravity wave field. These models of waves have been developed on the basis of observations of swell pattern in open ocean. The radar scattering from water is largely due to the roughness produced by the capillaries which results in Bragg effects, and is thus a surface phenomena.

In the case of ice there are no capillaries. The radar scattering from ice is not only influenced by the roughness of the surface but also by the subsurface structure

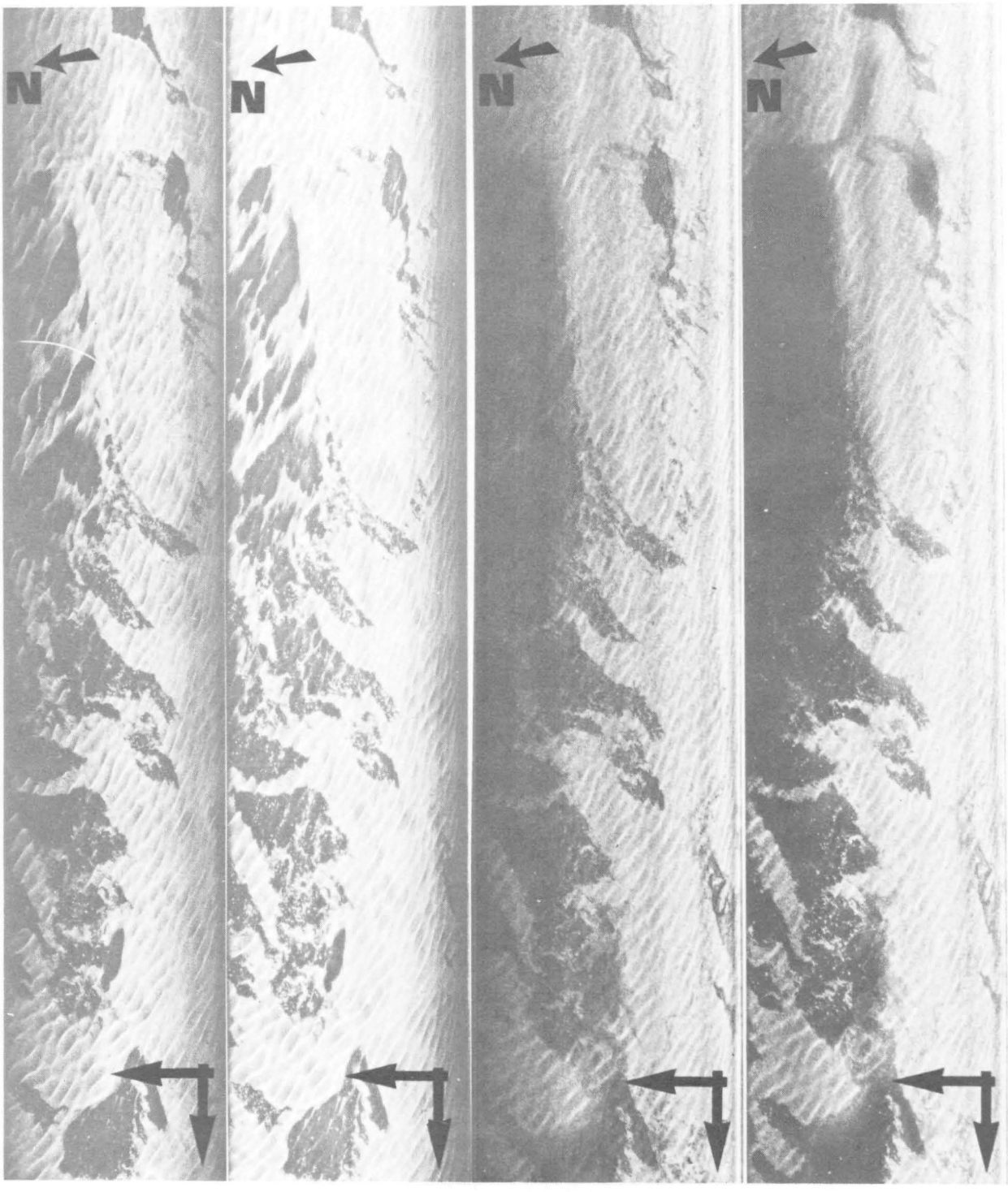

FIGURE 8 SAR IMAGERY, REGION AMOP 18, PASS 7;
X-BAND HV AND HH, L-BAND HV AND HH, FEBRUARY 25, 1977.
(Location Lat. 55°N, Long. 57°W)

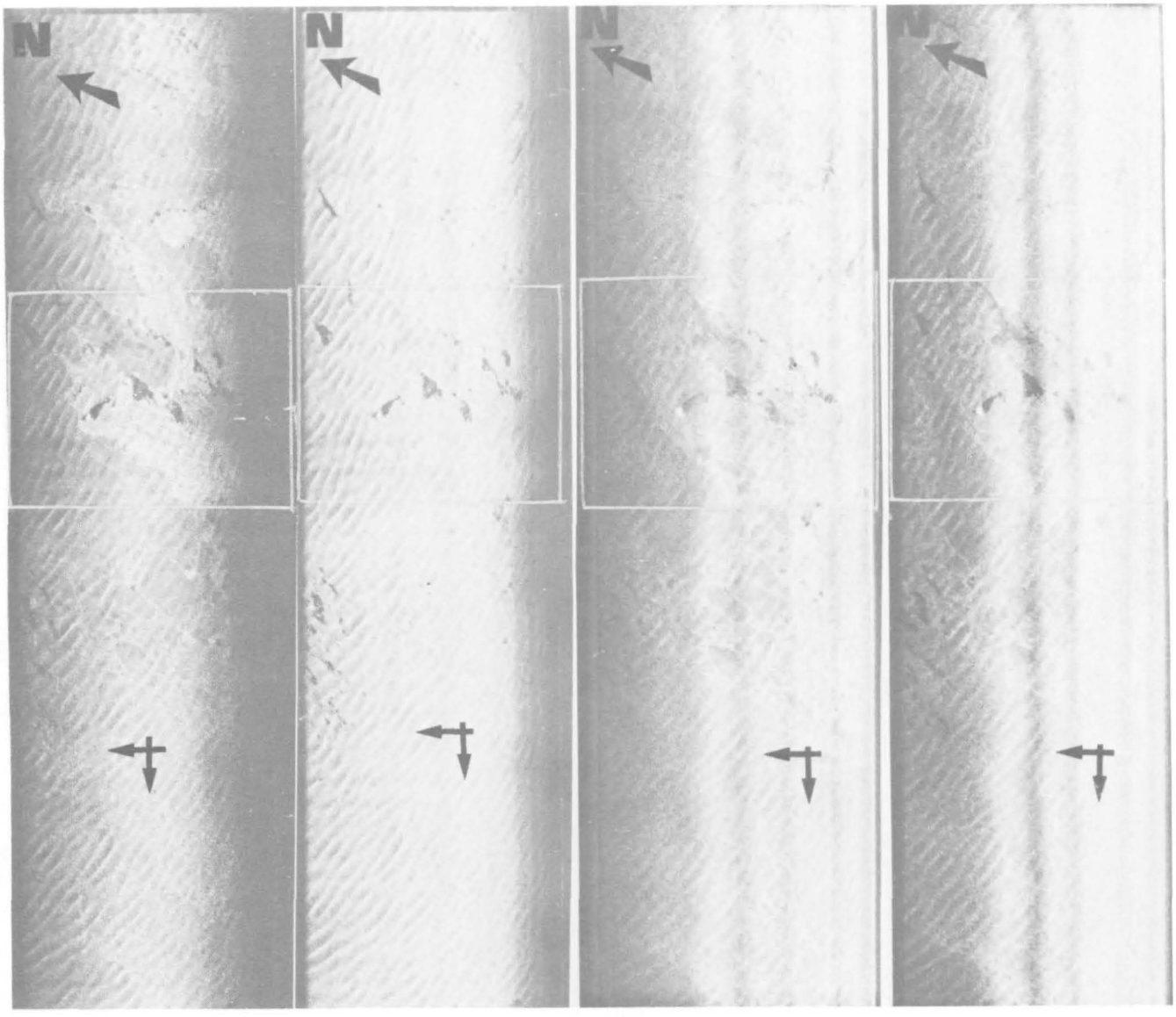

FIGURE 9 SAR IMAGERY, ICEBERG 1, PASS 3;
X-BAND HV AND HH, L-BAND HV AND HH, MARCH 13, 1977.
Note: Digitized areas are marked by rectangles.
(Location: Lat. 55°37'N, Long. 58°16'W)

especially for longer wavelengths. It is known that the capillary reflectivity is a function of the resolution cell's position on the gravity wave. Even if surface roughness is the primary mechanism of radar scattering from ice, it is difficult to see how the passage of the swell through ice can change the surface roughness and hence the reflectivity pattern, based on the cell's position on the gravity wave. As stated by Dawe and Parashar (1978), the variation in the intensity due to purely tilt modulation is about 2 dB which is too small to account for the observed variations on the radar imagery. In a flexible ice covered wavy surface, as stated by Raney and Lowry (1978), there is assurance that the dominant motion is up and down rather than transverse. As a result, the model developed by them which accounts for wave height modulation seems to be more applicable in the case of waves in ice. However, it appears difficult to explain the disappearance of waves in the dark toned areas on the basis of this model.

A wave whose velocity of propagation is controlled primarily by gravity is termed a gravity wave and water waves of a length greater than 5 cm are considered such. Capillary waves, also called ripples, have wavelengths less than 3 cm, and the velocity of propagation is primarily controlled by the surface tension of the liquid in which the wave is travelling. In open water, capillary waves are wind induced. The types of gravity waves which can propagate in ice and their associated attenuations are described by Bates (1978) and Bates and Shapiro (1978). Based on theoretical study, it is stated that the phase velocity of the gravity waves in the ice covered sea cannot exceed that in free surface water at the same frequency. The highest frequency that can be propagated is the resonant frequency of the system, for which the wave phase velocity in ice equals the free-surface phase velocity. The actual change in phase velocity encountered in ice depends on the flexural properties of ice.

In view of the above, as the phase velocity in water is more than that in ice, the disappearance of waves in open water could be due to defocusing. As stated by Shuchman et al (1977), a target moving at 12 m/sec in the along-track direction introduces shifts in the focal length of 0.579 mm for L-band and 1.264 mm for X-band. The depth of focus for the ERIM system are $\pm$0.0502 mm and $\pm$0.7804 mm for the 3 m resolution, L- and X-bands, respectively. As a result the X-band change is not detectable, because it is within the depth of focus. Refocusing is required for the L-band case. It is concluded that given the same wave velocity, defocusing of wave imagery due to along-track velocity components of waves is more pronounced at L-band than at X-band. For

the imagery presented; if the disappearing of waves is caused by defocusing as a result of differences in phase velocity, the defocusing is more apparent at X-band than at L-band.

A simpler explanation is that even after modulation due to swell, the returned energy from open water is below the noise level. Past results have shown that the difference in radar return from open water and ice in general is more at X-band than at L-band. For a wave to be visible on the radar imagery, its length should at least be 4 times the resolution cell size. For a resolution of 3 m x 3 m, the capillary wavelength is below the size of the resolution cell. From the resolution cell size and velocity considerations, therefore, the capillary wave structure cannot be discernible as such. It may be possible to pick up the modulations imported due to swell with overriding capillaries in open water if the data are processed for a target moving with a higher speed than the one chosen for the data presented here.

3.2 Region 2 - Iceberg 1

The corresponding aerial photograph for the ice area presented in Figure 9 is shown in Figure 37. A comparison of the two figures, shows that swell pattern in ice which is not apparent in the photo can be delineated in the radar image. The photo shows an iceberg surrounded by cakes of ice which is consolidated in some regions and partly consolidated in others. The digital data obtained from this radar image was used to determine signal to noise ratios and simple enhancement techniques were utilized to present grey-tone reproduction of radar image.

3.2.1 Digital Procedures. The 4-channel radar imagery presented in Figure 9 was digitized at ERIM producing 2306 x 1630 pixels for each channel corresponding to pixel size of 1.5 m x 1.5 m. The digitized data obtained from each channel are not registered so a pixel comparison between channels cannot be made. Channel to channel comparison is also precluded because of the uncalibrated nature of the original radar data as a result of different transmitted power levels, gain adjustments, and antenna patterns. Prior to 8-bit digitization of the intensity value, the square-root of the video was taken. The resulting data have been normalized to the laser power level.

To find the relationship between the digitized grey-tone level of the original intensity value and that obtained from the digitization of the square-root of the intensity value, consider the following:

Let "I" be the original intensity value for which grey-tone digitized level has to be found between 0 and 255. If "I_m" is the intensity value associated with the highest

digitized value of 255, then that implies the intensity range from 0 to I_m is divided equally into 256 levels. As a result, the digitized grey-tone level "I_d" corresponding to the intensity value of I is:

$$I_d = 255 \frac{I}{I_m} \tag{1}$$

Now if the square-root of intensity "I" was taken prior to digitization the corresponding grey-tone level "I_{ds}" is:

$$I_{ds} = 255 \frac{\sqrt{I}}{I_{ms}} \tag{2}$$

where, "I_{ms}" is the maximum value of intensity associated with level 255. Equation 2, can be written as:

$$I_{ds}^2 = (255)^2 \frac{I}{I_{ms}^2} \tag{3}$$

By eliminating "I" between equations (1) and (3), we have:

$$I_d = \frac{I_{ds}^2}{255} \frac{I_{ms}^2}{I_m} \tag{4}$$

It is reasonable to assume that $I_m = I_{ms}$, because the square-root was taken in order to handle larger values of intensities. This implies that I_m or I_{ms} correspond to the maximum value of the intensity that can be accommodated by the digitizing system, and therefore;

$$I_d = I_{ds}^2 \frac{I_m}{255} \tag{5}$$

This relationship shows that taking square of the available digitized grey-tone levels (corresponding to square-root of intensity values) is more appropriate, as it provides better reproduction of the original intensity data. The factor of $I_m/255$ being a constant will not change the relative evaluation of the obtained data, but non-squaring of obtained data may produce erroneous results.

3.2.2 Grey-tone Image Generation. The computer system used to generate grey-tone images from the digital data consisted of a HP 2100S mini-computer having a core of 34K, a 7900A disc unit consistintg of a system disc and a user mountable disc, two HP 7970E 1600 bpi magnetic tape units, a HP 9866A lineprinter, a Tektronix 4010-1 video keyboard and an ANAC 911 graphic recorder.

The grey-tone images presented here were produced on dry electrosensitive paper through the ANAC recorder. The system reproduces 16 grey-tone levels with 0 corresponding to white and 15 to black.

3.2.3 Histograms. The first step in the analysis of the digital data was to produce histograms of the grey-tone values for selected areas on the radar image. The approximate areas for which histograms are produced are shown in Figure 10. The largest area corresponded to about 100 x 150 pixels or about 150 x 225 m. Care was taken to consider more pixels in the azimuth direction than in the range-direction so as to avoid averaging over the range. The most difficult aspect of this task was accurately locating the same areas on all the channels and finding the corresponding coordinates on the digital tape. The X-band, HV image shown in Figure 10 was taken as a reference. Areas were marked on this image and their coresponding location on the digital image was noted. This required repeated reproduction of the grey-tone image for the selected areas. As the digital data from each channel are stored on a separate file and the corresponding files are not registered, determination of the location of the same area on each channel and the corresponding pixel coordinates required repeated generation of grey-tone images. Considerable care was taken to produce histograms for each channel from the same area. The generated histograms are shown in Figures 11 through 19. The frequency value noted on the histograms is normalized to a population of 1000. The grey-tone levels available on the magnetic tape were squared and are represented as grey scale values on the graphs. The points marked on graphs correspond to actual values obtained and a smooth line is drawn through the points to show the shape.

Because of the height of the iceberg, there is a region of shadow behind it labelled in Figure 10. The histograms for the 4-channels for the shadow region are shown in Figure 11. The peak of the distribution for the X-band, HV channel is at zero and the second maximum occurs at about 35. There does not appear to be much difference between the shape of the two curves for the X-band, HH and HV channels. The curves for the two L-band channels are distinctly different than those for the X-band. Both L-band curves are very similar, containing more grey scale values than X-band, and are relatively broader in shape. The peaks for L-band channels occur at a grey scale value of about 200.

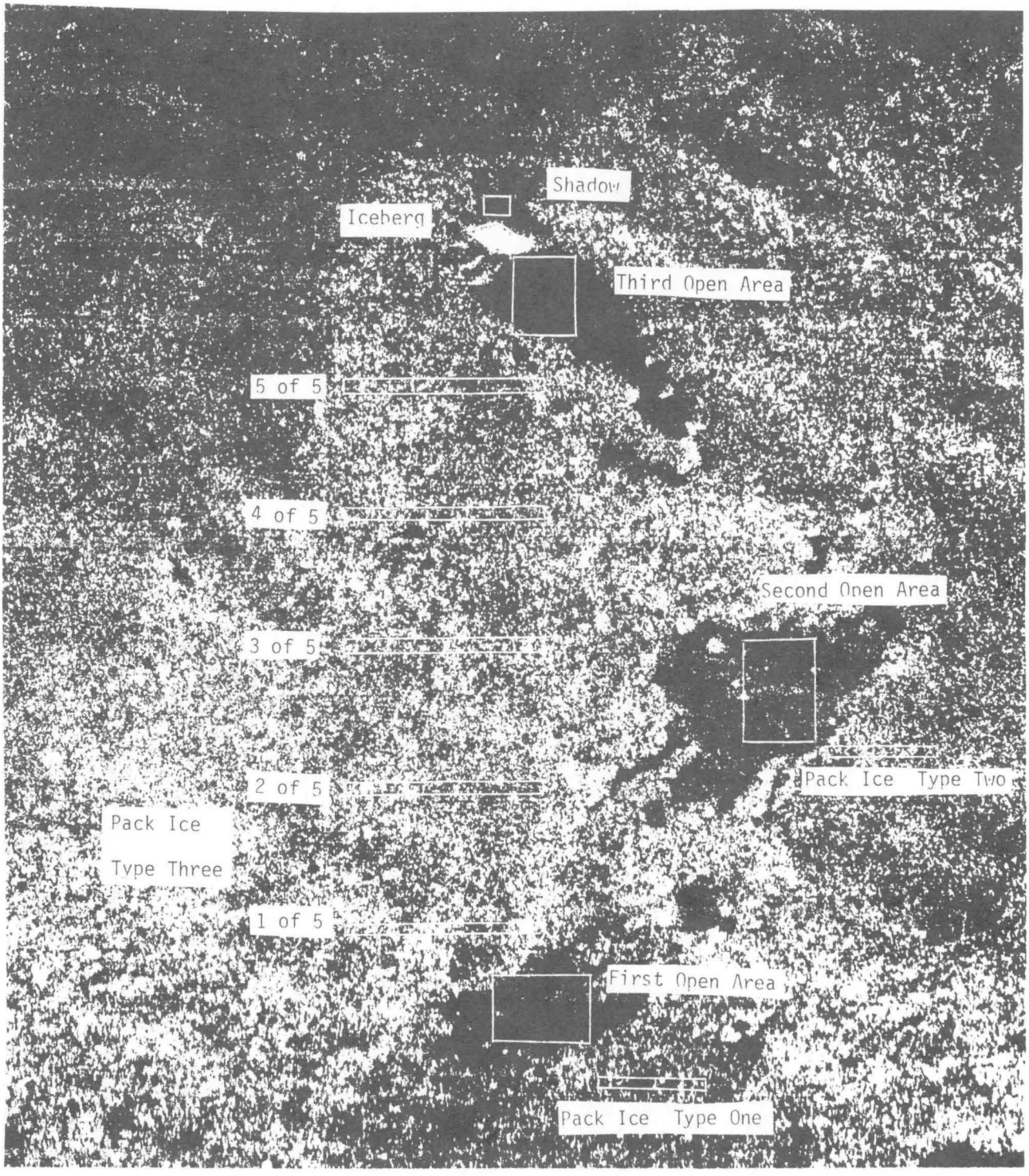

FIGURE 10 LOCATION OF AREAS ON THE IMAGERY THAT WERE USED TO GENERATE THE HISTOGRAMS

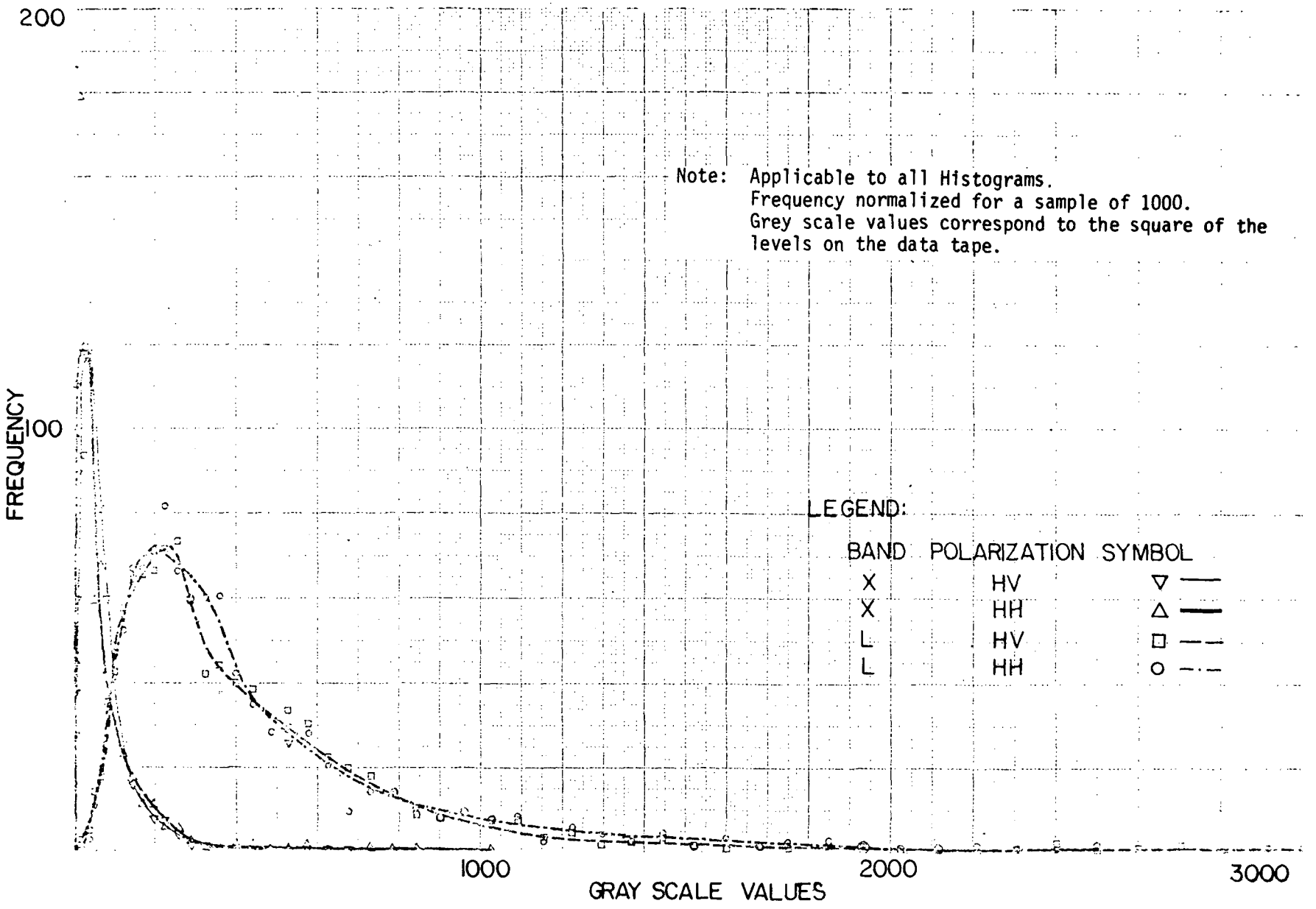

FIGURE 11 HISTOGRAM OF THE SHADOW AREA

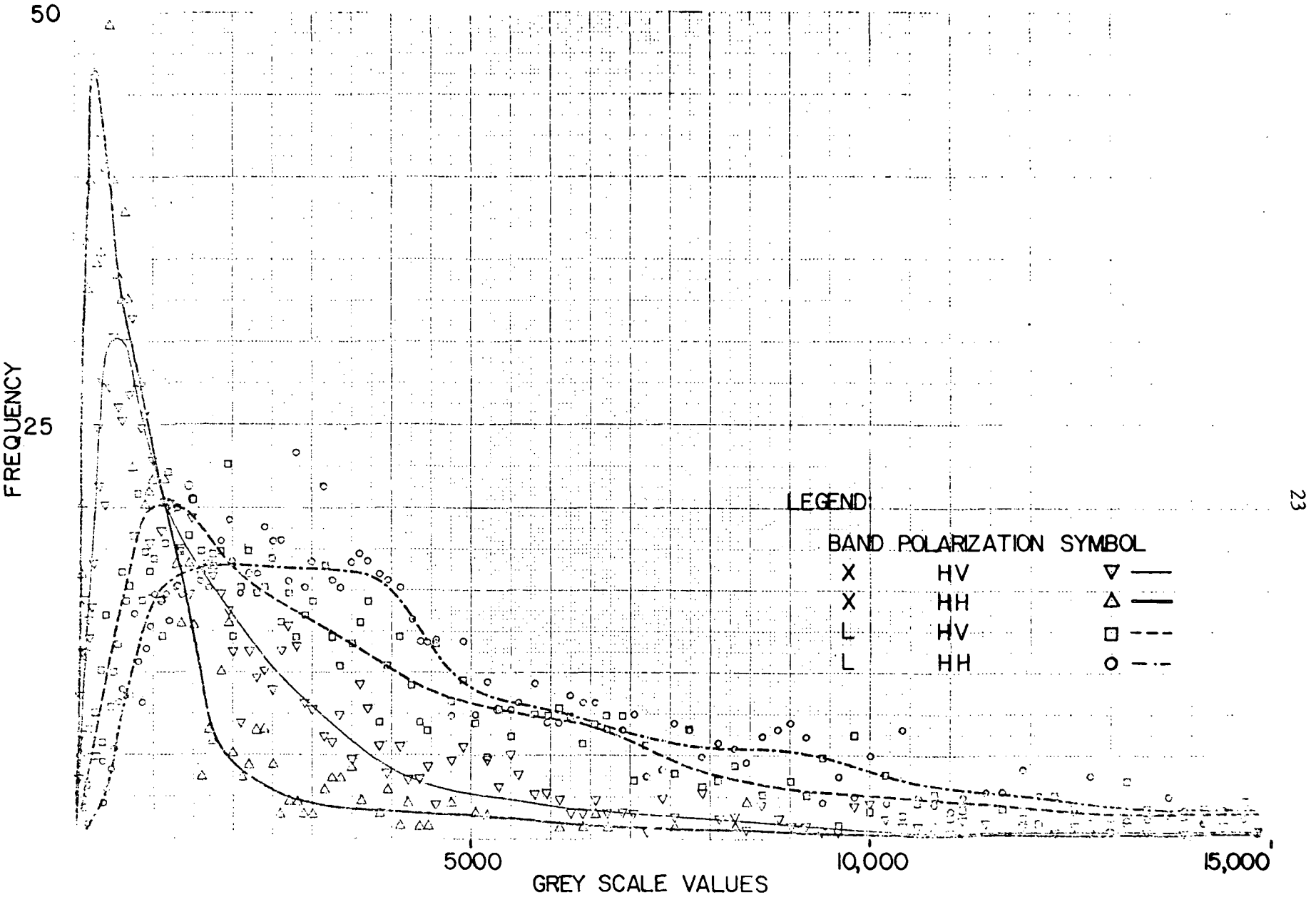

FIGURE 12 HISTOGRAM OF THE ICEBERG AREA

The histograms for the 4-channels corresponding to the iceberg area are shown in Figure 12. The shape of the two X-band channels is again similar; but the shape of the two L-band channels differs slightly. The X-band curves have a narrower peak as compared to L-band curves.

The histograms for the three pack ice type areas corresponding to X-HV, X-HH, L-HV, and L-HH are shown respectively in Figures 13, 14, 15, and 16. The histograms for the Ice Type 3 was prepared by combining histograms for the five areas shown in Figure 10. The three ice types show similar shape on the two X-band channels, however, there is a difference between the two channels. The two L-band channels have slightly different shapes.

The four histograms for first dark area are shown in Figure 17, for the second dark area in Figure 18, and for the third dark area in Figure 19. For the second dark area the X-HV and L-HH curves almost overlap. The two X-band and L-band curves for the first and third dark areas appear different. The peak for the third dark area corresponding the two X-band channels is at zero.

A comparison of the histograms presented above indicates that the shape of the distribution for the two X-band channels remains similar from region to region. The distribution has a narrow peak with most of the values around this peak. The shape of the curves for the two L-band channels differs for different areas. The distribution has a broader peak and grey-tone values cover a large range.

3.2.4 Statistics of Radar Return. Radar images are speckled in nature because of scintillation in fading resulting from phase interference. Each resolution cell can be thought of as a collection of independent scatterers. The size of the phasor sum of the fields due to the different scatterers depends upon their relative distances and consequently upon the look angle. Either the noise or the radar signal may be thought of as the sum of sine and cosine components whose amplitudes are independent and statistically determined by a Gaussian distribution. As stated by Moore (1976), use of this type of distribution presumes that each pixel contains a large number of independent scatterers and that no single scatterer contributes a signal to the comlex that is large compared with the total power contributed by all the scatterers in the complex. For large pixels and area-extensive targets, this is a reasonable assumption based on experimental evidence. The probability that some individual scatterer will dominate becomes greater as the pixel becomes smaller. The assumption appears to hold down to a resolution of the order of 3 m. The voltage envelope of this type of received signal is "Rayleigh" distributed and

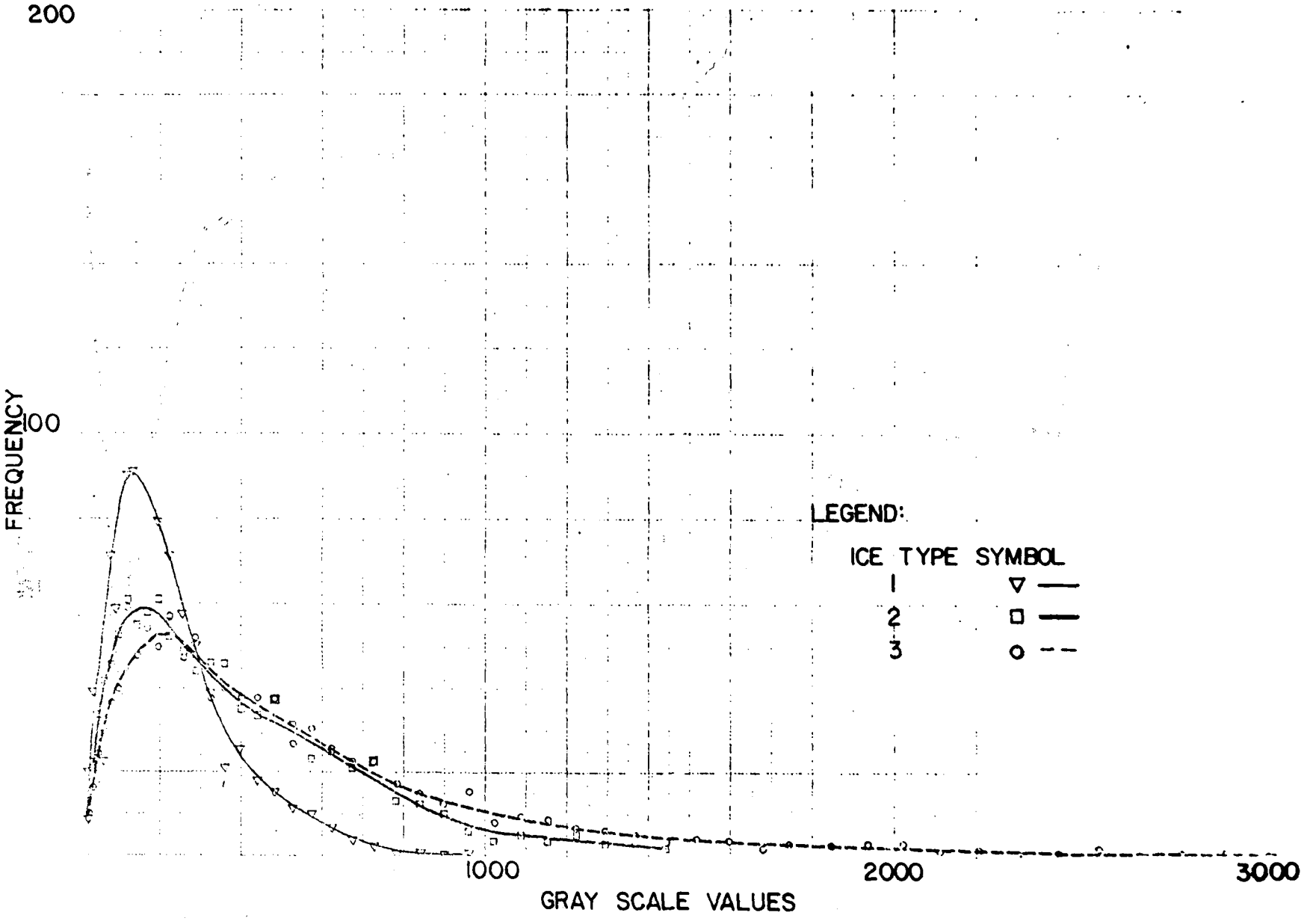

FIGURE 13 HISTOGRAM OF THE THREE X-BAND HV ICE TYPES

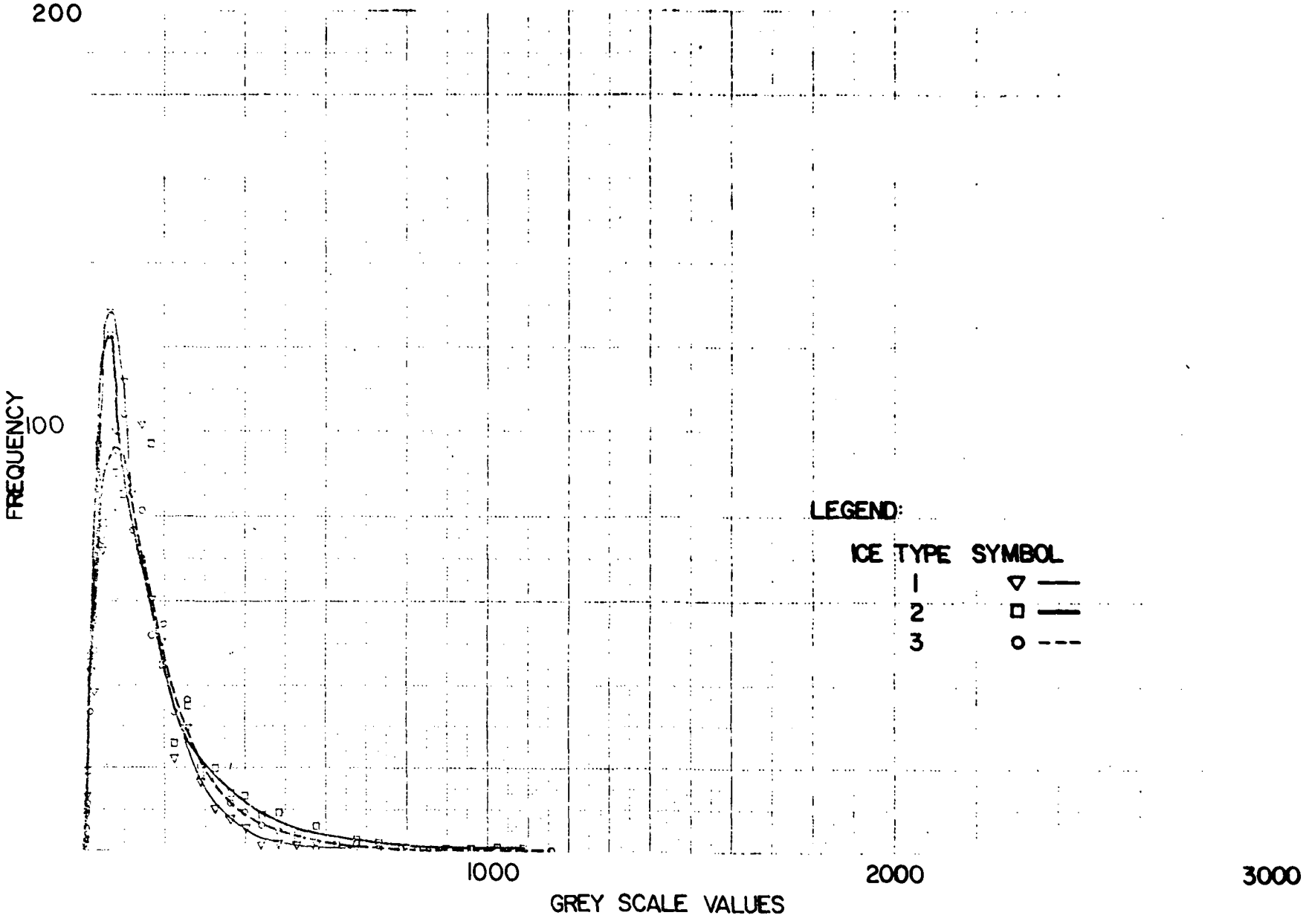

FIGURE 14 HISTOGRAM OF THE THREE X-BAND HH ICE TYPES

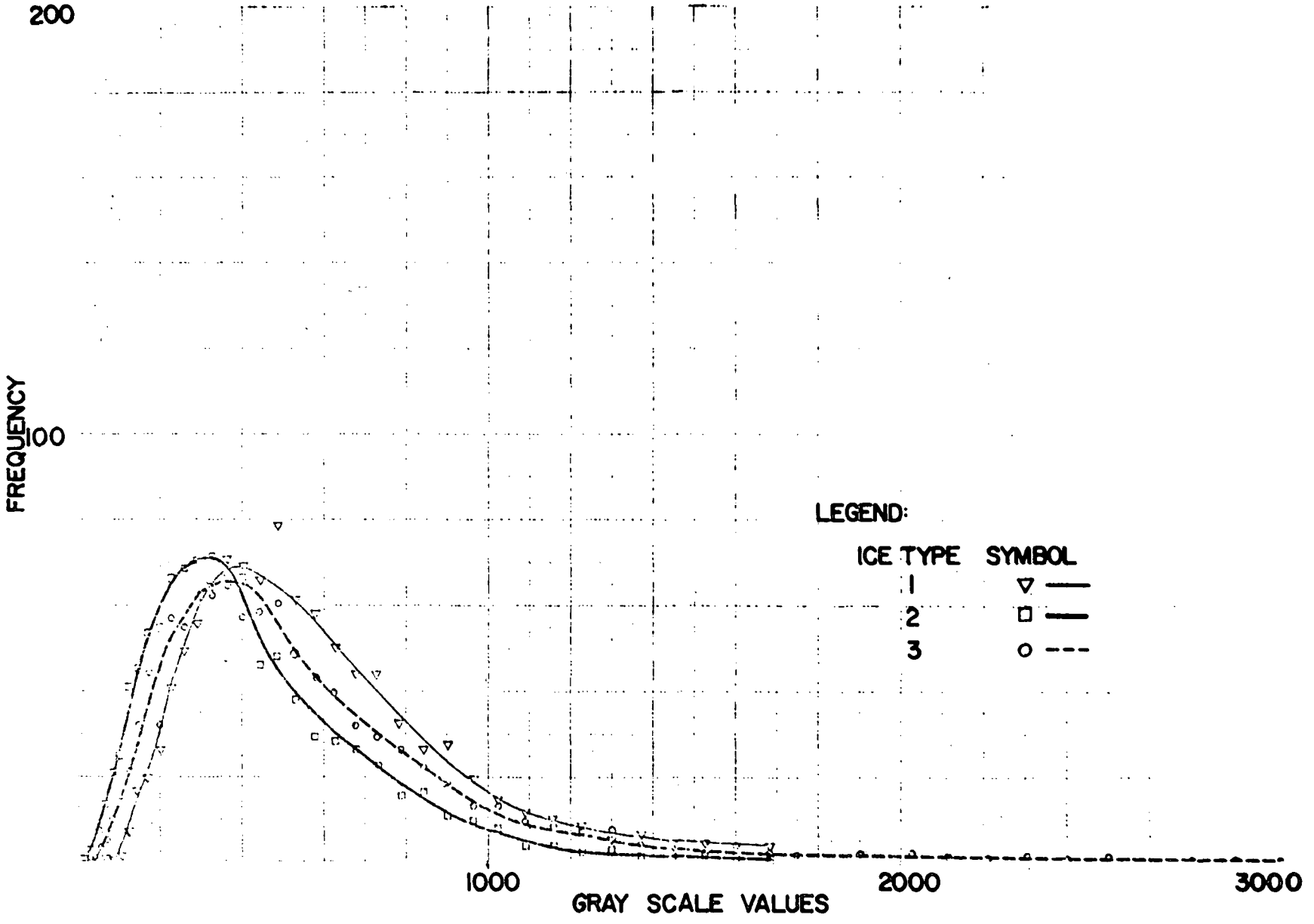

FIGURE 15 HISTOGRAM OF THE THREE L-BAND HV ICE TYPES

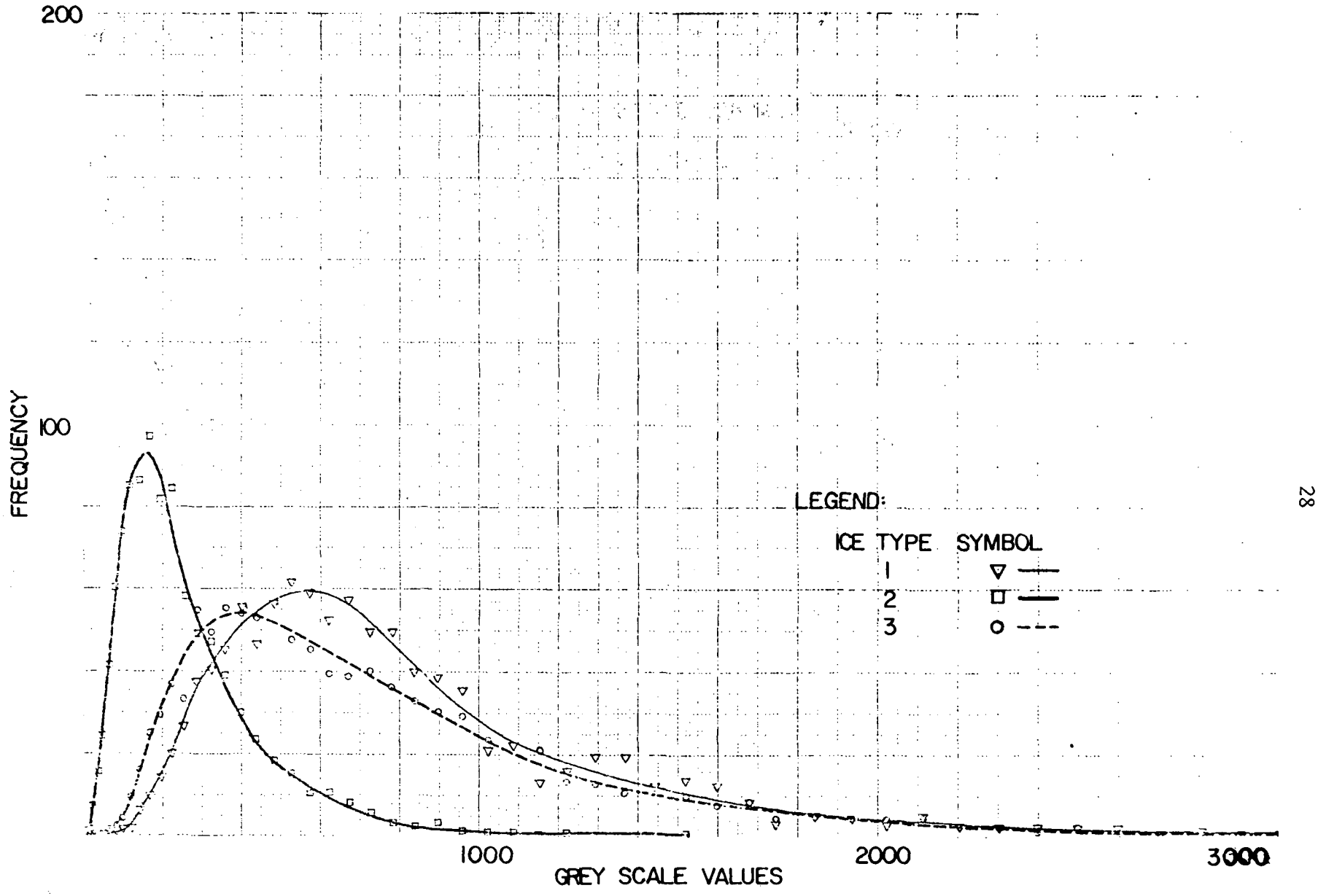

FIGURE 16 HISTOGRAM OF THE THREE L-BAND HH ICE TYPES

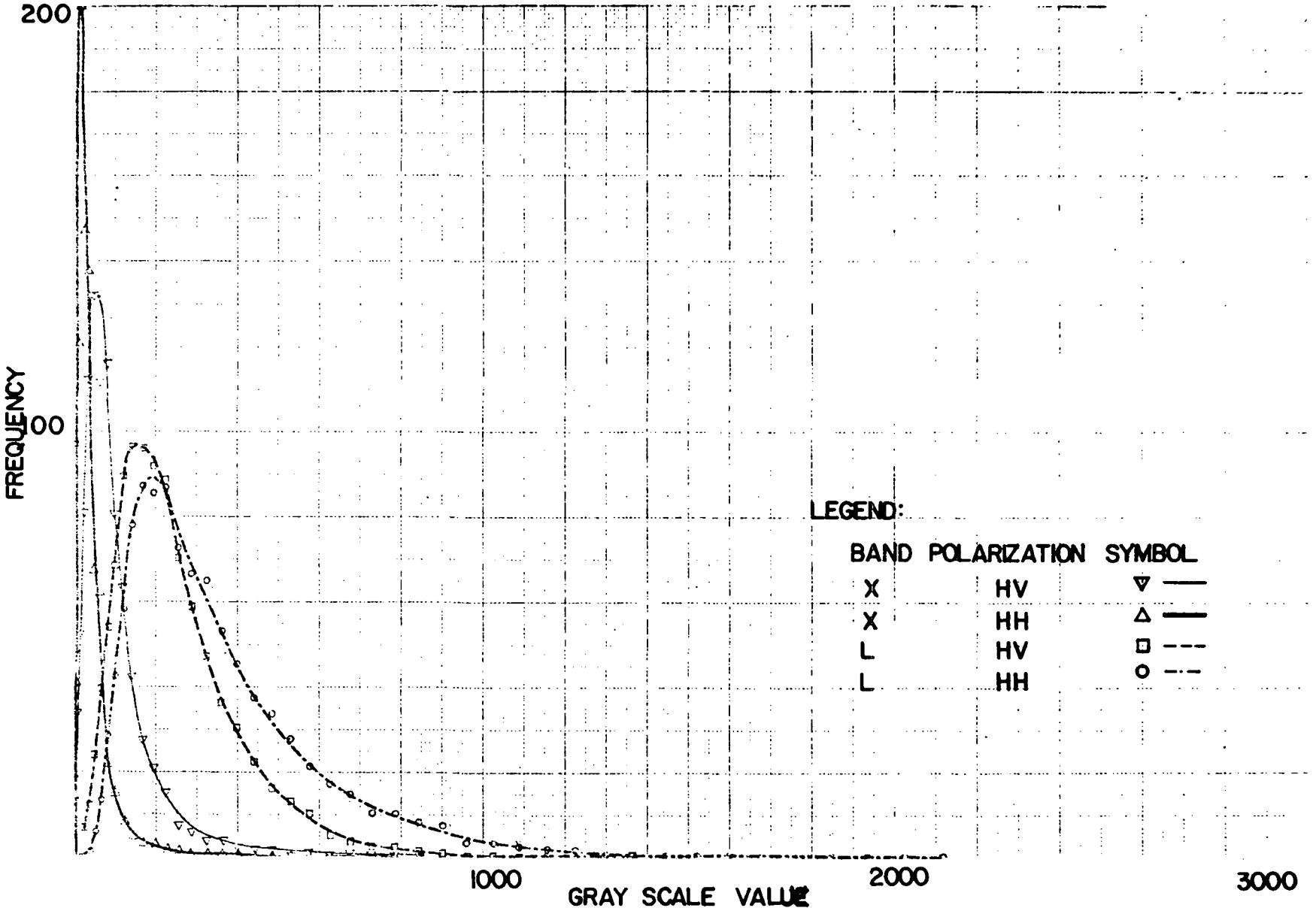

FIGURE 17 HISTOGRAM OF THE FIRST OPEN WATER AREA

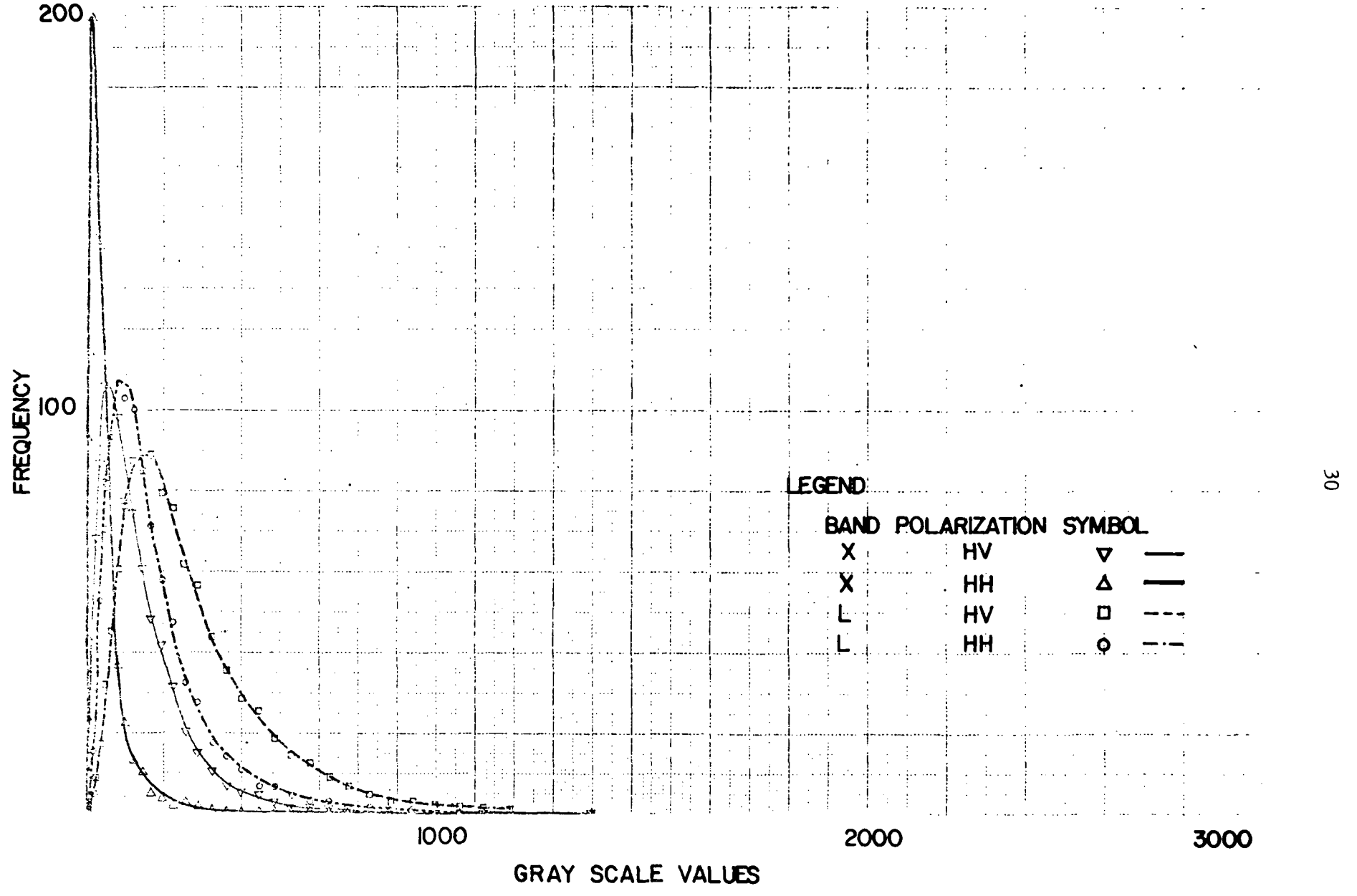

FIGURE 18 HISTOGRAM OF THE SECOND OPEN WATER AREA

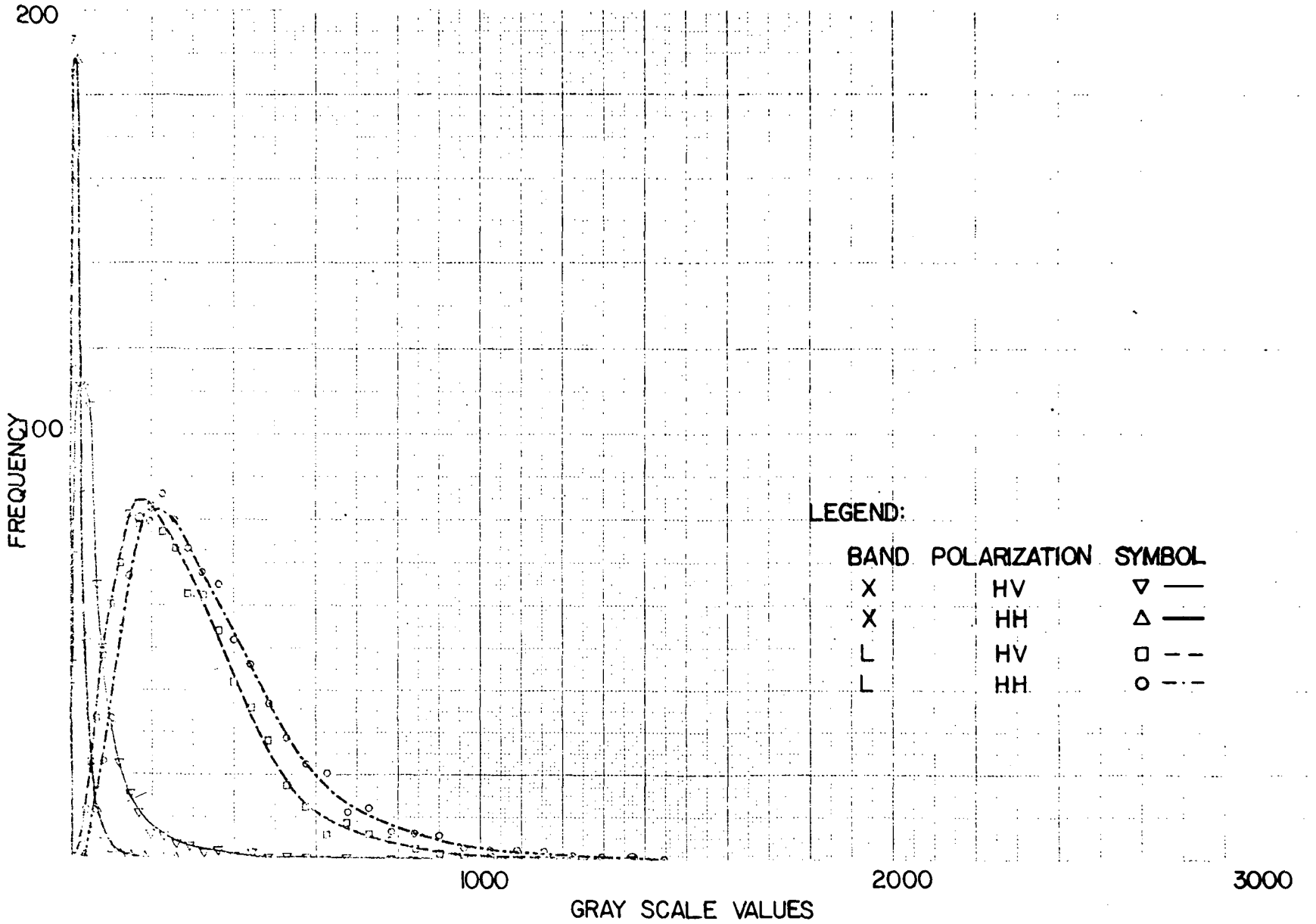

FIGURE 19 HISTOGRAM OF THE THIRD OPEN WATER AREA

after square law detecting its power is exponentially distributed. Each pulse return is a single sample from this distribution. The standard deviation and mean for the exponential distribution is equal. This implies that individual samples may be widely distributed about the mean which results in a speckled appearance, where the signals much stronger than the mean make bright spots on the image and those much weaker, make dark spots.

The speckling may be reduced by averaging several independent samples of this exponential distribution. The averaging of N samples produces a chi-squared distribution of 2N degrees of freedom. The exponential distribution is a chi-squared distribution of two degrees of freedom. The standard deviation for an average of N samples is

$$\sigma N = \frac{U_N}{\sqrt{N}} \tag{5}$$

where, U_N is the sample mean, and N is the number of independent samples. The independent samples can be combined either along the flight track or in the range direction. The number of independent samples along-track are given by:

$$N = \frac{\text{resolution in azimuth}}{D/2}$$

where D is the physical dimension of the antenna. For a fully focused synthetic aperture radar where the azimuth resolution is D/2, only one independent sample is obtained.

The histograms presented in the preceding section do have chi-squared distribution in general. Some actually appear to be Rayleigh distributed possibly because of the small number of independent samples.

The statistics of the grey-tone values for the areas marked on Figure 10 were obtained. These were produced for both the squared and non-squared cases. As the sum of the squares and square of the sum produce different values, it was decided to compute both. The results for the 4-channels corresponding to squared and unsquared data respectively are provided in Tables I and II. The squared data correspond to the square of the grey-tone values and unsquared correspond to just the value on the tape. The mean, standard error, mode, standard deviation, minimum and maximum value, and population size are presented in the tables. The standard error is generally defined as the standard error of the mean and is approximately equal to the standard deviation divided by the

TABLE I SQUARED DATA STATISTICS

Classification		Mean	Standard Error of Mean	Mode	Standard Deviation	Minimum	Maximum	Population
Channel 1, X-HV								
Shadow		44.322	1.268	784	56.333	0	676	1963
Iceberg		1882.096	56.462	0	2864.038	16	33856	2573
First Open Water		74.644	0.570	49	69.124	0	841	14734
Second Open Water		100.600	0.810	49	99.496	0	1600	15100
Third Open Water		41.694	0.594	0	63.750	0	961	11493
Pack Ice - Type 1		187.792	2.696	144	136.456	1	961	2560
- Type 2		317.134	5.500	196	278.242	0	2916	2560
- Type 3	- 1 of 5	999.330	6.612	225	458.114	0	4225	4800
	- 2 of 5	321.276	5.472	121	309.522	0	3969	3200
	- 3 of 5	456.492	7.298	225	505.588	0	6561	4800
	- 4 of 5	341.294	5.122	196	354.900	0	4356	4800
	- 5 of 5	317.348	4.296	169	297.596	0	3721	4800
Channel 2, X-HH								
Shadow		42.836	1.214	16	68.998	0	1024	3235
Iceberg		816.404	26.102	441	983.928	25	10816	1421
First Open Water		29.610	0.376	16	40.042	0	694	11300
Second Open Water		37.032	0.596	16	73.326	0	2809	15100
Third Open Water		12.168	0.180	16	15.738	0	256	7695
Pack Ice - Type 1		109.512	1.610	64	81.414	0	676	2560
- Type 2		124.976	2.480	64	125.526	0	1089	2560
- Type 3	- 1 of 5	109.540	0.914	64	70.738	4	784	6000
	- 2 of 5	124.310	1.402	64	108.658	0	1156	6000
	- 3 of 5	145.054	1.670	64	132.562	0	1444	6300
	- 4 of 5	120.370	1.398	64	108.338	0	1296	6000
	- 5 of 5	98.420	1.200	64	92.932	0	900	6000

TABLE I SQUARED DATA STATISTICS (cont'd)

Classification		Mean	Standard Error of Mean	Mode	Standard Deviation	Minimum	Maximum	Population
Channel 3, L-HV								
Shadow		363.002	7.026	256	350.714	9	3249	2492
Iceberg		3721.508	105.608	1936	5066.998	14	63504	2302
First Open Water		216.308	1.323	144	140.962	0	1369	11300
Second Open Water		222.938	1.382	169	169.760	0	1849	15100
Third Open Water		244.848	2.118	196	157.728	0	1369	5545
Pack Ice - Type 1		529.040	5.620	484	284.398	64	1764	2560
- Type 2		373.958	4.806	324	243.186	4	1681	2560
- Type 3	- 1 of 5	545.698	5.726	361	396.848	16	2704	4800
	- 2 of 5	479.724	4.936	361	342.096	16	3364	4800
	- 3 of 5	540.410	5.980	361	414.368	9	4761	4800
	- 4 of 5	542.094	5.626	324	389.790	4	4096	4800
	- 5 of 5	404.742	4.170	361	288.844	16	2601	4800
Channel 4, L-HH								
Shadow		363.180	5.660	225	327.428	9	3136	3346
Iceberg		4225.562	87.638	2809	4331.708	121	42026	2443
First Open Water		304.400	1.974	169	209.806	9	2116	11300
Second Open Water		141.032	0.982	81	120.582	0	1764	15100
Third Open Water		306.184	2.574	225	191.626	4	1444	5545
Pack Ice - Type 1		721.482	8.766	529	443.486	49	3136	2560
- Type 2		227.322	3.302	169	167.056	0	1521	2560
- Type 3	- 1 of 5	787.130	8.984	484	622.452	49	5041	4800
	- 2 of 5	655.610	6.736	484	466.748	25	3844	4800
	- 3 of 5	479.850	5.732	225	391.144	16	4096	4800
	- 4 of 5	660.650	6.476	529	448.702	64	4356	4800
	- 5 of 5	603.320	5.876	289	407.090	36	3025	4800

TABLE II STATISTICS OF UNSQUARED DATA

Classification		Mean	Standard Error of Mean	Mode	Standard Deviation	Minimum	Maximum	Population
Channel 1, X-HV								
Shadow		5.390	0.088	0	3.908	0	26	1963
Iceberg		36.975	0.477	28	22.697	4	104	2573
First Open Water		7.804	0.031	7	3.707	0	29	14734
Second Open Water		8.957	0.037	7	4.514	0	40	15100
Third Open Water		5.061	0.037	0	4.010	0	31	11495
Pack Ice - Type 1		17.859	0.094	12	4.739	1	31	2560
- Type 2		16.284	0.143	14	7.210	0	54	2560
- Type 3	- 1 of 5	20.585	0.126	15	8.696	0	65	4800
	- 2 of 5	18.607	0.136	11	9.395	0	87	4800
	- 3 of 5	19.114	0.138	15	9.548	0	81	4800
	- 4 of 5	16.710	0.114	14	7.879	0	66	4800
	- 5 of 5	16.285	0.104	13	7.223	0	61	4800
Channel 2, X-HH								
Shadow		5.412	0.065	4	3.681	0	32	3235
Iceberg		25.631	0.350	21	13.021	5	104	1381
First Open Water		4.715	0.026	4	2.717	0	28	11300
Second Open Water		5.214	0.026	4	3.138	0	53	15100
Third Open Water		2.812	0.024	4	2.064	0	16	7695
Pack Ice - Type 1		9.783	0.073	8	3.717	0	26	2560
- Type 2		10.077	0.096	8	4.841	0	33	2560
- Type 3	- 1 of 5	10.016	0.039	8	3.038	2	28	6000
	- 2 of 5	10.294	0.055	8	4.284	0	34	6000
	- 3 of 5	19.231	0.114	15	9.026	0	61	6300
	- 4 of 5	10.109	0.055	8	4.263	0	36	6000
	- 5 of 5	7.841	0.060	7	4.636	0	29	6000

TABLE II STATISTICS OF UNSQUARED DATA (cont'd)

Classification		Mean	Standard Error of Mean	Mode	Standard Deviation	Minimum	Maximum	Population
Channel 3, L-HV								
Shadow		17.577	0.147	16	7.354	3	57	2492
Iceberg		53.310	0.618	44	29.664	7	252	2302
First Open Water		14.022	0.042	12	4.444	0	37	11300
Second Open Water		14.040	0.041	13	5.082	0	43	15100
Third Open Water		14.881	0.065	14	4.838	0	37	5545
Pack Ice - Type 1		22.234	0.116	22	5.862	8	42	2560
- Type 2		18.393	0.118	18	5.974	2	41	2560
- Type 3	- 1 of 5	22.027	0.112	19	7.779	4	52	4800
	- 2 of 5	20.766	0.101	19	6.965	4	58	4800
	- 3 of 5	21.882	0.113	19	7.849	3	69	4800
	- 4 of 5	22.048	0.108	18	7.482	2	64	4800
	- 5 of 5	19.040	0.094	19	6.498	4	51	4800
Channel 4, L-HH								
Shadow		17.702	0.122	15	7.058	3	56	3346
Iceberg		59.140	0.546	53	26.987	11	205	2443
First Open Water		16.600	0.051	13	5.369	3	46	11300
Second Open Water		11.058	0.035	9	4.331	0	42	15100
Third Open Water		16.748	0.068	15	5.069	2	38	5545
Pack Ice - Type 1		25.755	0.151	23	7.626	7	56	2560
- Type 2		14.221	0.099	13	5.009	0	39	2560
- Type 3	- 1 of 5	26.292	0.141	22	9.792	7	71	4800
	- 2 of 5	24.245	0.119	22	8.233	5	62	4800
	- 3 of 5	20.457	0.113	15	7.835	4	64	4800
	- 4 of 5	24.483	0.113	23	7.827	8	66	4800
	- 5 of 5	23.365	0.109	17	7.578	6	55	4800

square-root of the population size. In a sense it is normalized standard deviation. The mode refers to the grey scale value at which the peak in the histogram occurs.

The value of mean presented in the Table I shows that the mean for the five areas under Pack Ice Type 3 does not fall off with angle as it should. This is due to the antenna pattern. The iceberg region gives the highest mean, followed by pack ice areas, "open water" and shadow. For both the L-band channels, the return from "open water" areas is less than the shadow. The value of mean is the same order as the standard deviation and in certain cases such as iceberg and shadow, the standard deviation is more than the mean. The ratio of the two produce about one independant sample in accordance with equation 5. The assumption of equation 5 probably does not hold true for the iceberg and shadow region. Apart from the shadow and the iceberg regions, the maximum standard error is produced for the pack ice types. This probably represents variance in addition to fading due to the variations in the ice conditions. The equal mode for pack ice types in channel X-HH is to be noted. This helps to explain lack of tonal contrast in the ice types on the X-HH imagery.

3.2.5 Digital Grey-tone Images. The grey-tone images from the digital data on the tape were produced using the ANAC graphic recorder. Sixteen grey-tones can be reproduced through this recorder. As a result, 256 grey-tone levels on the tape in the range from 0 to 255 had to be reduced to sixteen levels in the 0 to 15 range. The zero level on the recorder corresponded to white and 15 to black. But on the tape, the level of 255 corresponded to white and 0 to black. As a result, the actual data had to be flipped over so as to produce the correct tonal representation.

There are two ways to reduce the 256 levels into 16. One is known as equal interval quantization, that is, the range 0 to 255 is divided into 16 equal intervals. As a result, the data point in the interval 0 to 15 was assigned a grey-tone level of 15, 16 to 31 a level of 14, and so on. The other method is known as equal density quantization. This involves producing histograms of the original data; then depending on the shape of the distribution, dividing the total range into 16 unequal intervals such that number of points falling in each interval is the same.

Both the mentioned methods were tried for the squared and unsquared data. It is possible to write an algorithm to implement the second method, but this was not done, here. The second method was implemented here through manually dividing the distribution curve in 16 unequal intervals, producing the grey-tone image, and updating the intervals to achieve better imagery.

The four images obtained with equal interval quantization for the unsquared data are shown in Figures 20 through 23. The actual image consisted of 2306 x 1630 pixels as shown in the File Label at the bottom. Only 2048 x 1630 pixels could be accommodated on the page. The histogram of all the areas produced showed that the maximum value available was smaller than 255. Combined histograms of the total data on one channel were not produced, so combined histograms of the pack ice areas were taken for the reference histogram. The top 10% of the population and the bottom 10% were assigned a level of 0 and 15 respectively. The remaining range was divided into 14 equal intervals. The top line of the image heading gives the assigned grey-tone levels. The line below this provides the ranges of the original data to which these levels were assigned. For Figure 20, X-HV image, grey-tone values from 0 to 12 were assigned a level of 15, 13 to 23 assigned level 14, 24 to 35 assigned level 13, 36 to 46 assigned level 12, 47 to 58 assigned level 11, 59 to 69 assigned level 10, and so on up until 173 to 255 were assigned level 0. The same procedure was followed for the other three channels. This procedure did not yield imagery of high quality.

The same method was used to produce images with the square data for equal interval quantization. The results for the 4-channels are presented in Figures 24 through 27. The quality of imagery is better than before, but major regions, (except icebergs) still cannot be distinguished.

The next step was to produce images with unequal interval quantization or equal density quantization. Only the best images produced are presented here. The 4-channels corresponding to unsquared data are shown in Figures 28 through 31. In Figure 28 as the label at the bottom of the image shows, grey-tone values from 0 to 9 were assigned a level of 15, 10 to 11 a level of 14, 12 to 13 a level of 13, and so on until values 28 to 255 were assigned a level of 0. The quality of imagery produced is much better than in the previous cases. The quality is comparable to photographic images and in some cases even better.

The imagery for the 4-channels corresponding to the squared data using the unequal interval quantization is provided in Figures 32 to 35. The quality is comparable to that for the unsquared case and certain features are more enhanced than others. However, there is not expected to be much difference between the unsquared and the squared case when unequal interval quantization is used. There is a difference between the two when only equal interval quantization is used.

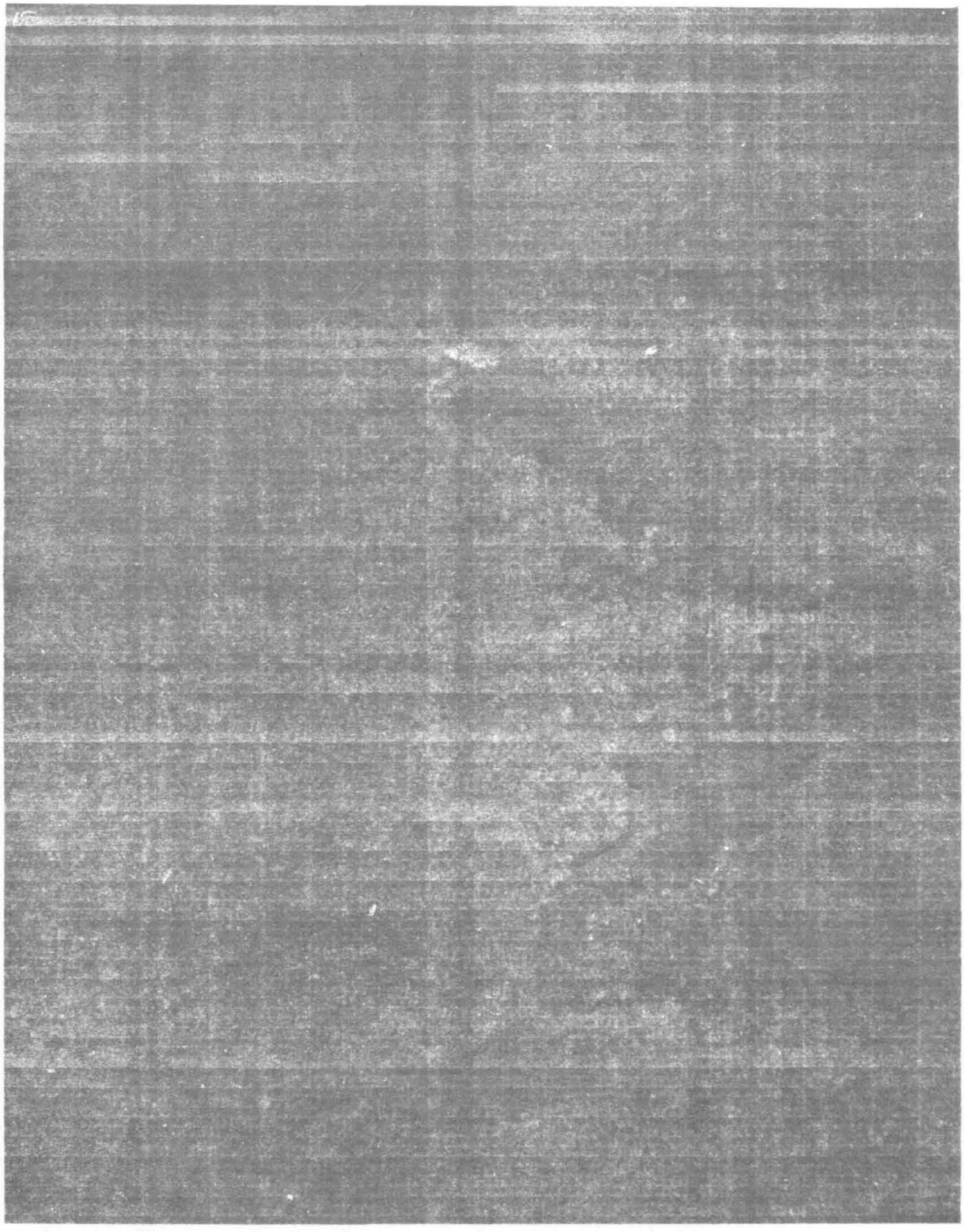

FIGURE 20 CHANNEL 1 UNSQUARED DATA, LINEAR GREY SCALE DISTRIBUTION

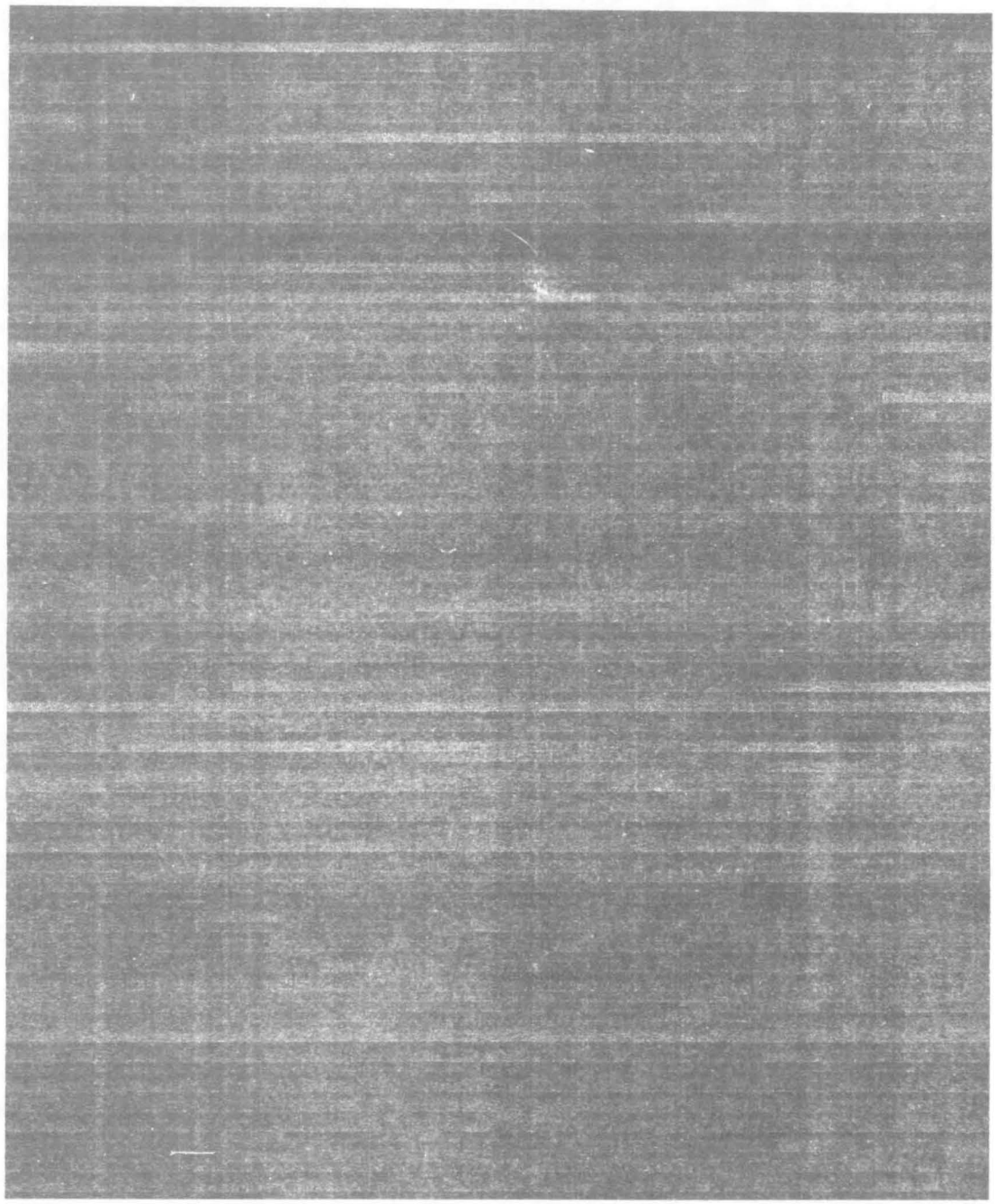

151413121110 9 8 7 6 5 4 3 2 1 0
7 13 20 26 33 39 46 52 59 65 72 78 85 91 98255
2 1 2048 1 1630 1
IPL 428 FILE 3 FLIGHT 3-13-77 PASS 3 X-BAND HH ICEBERG 2306X1630 1.5M/P1X SQRT 1

FIGURE 21 CHANNEL 2 UNSQUARED DATA, LINEAR GREY SCALE DISTRIBUTION

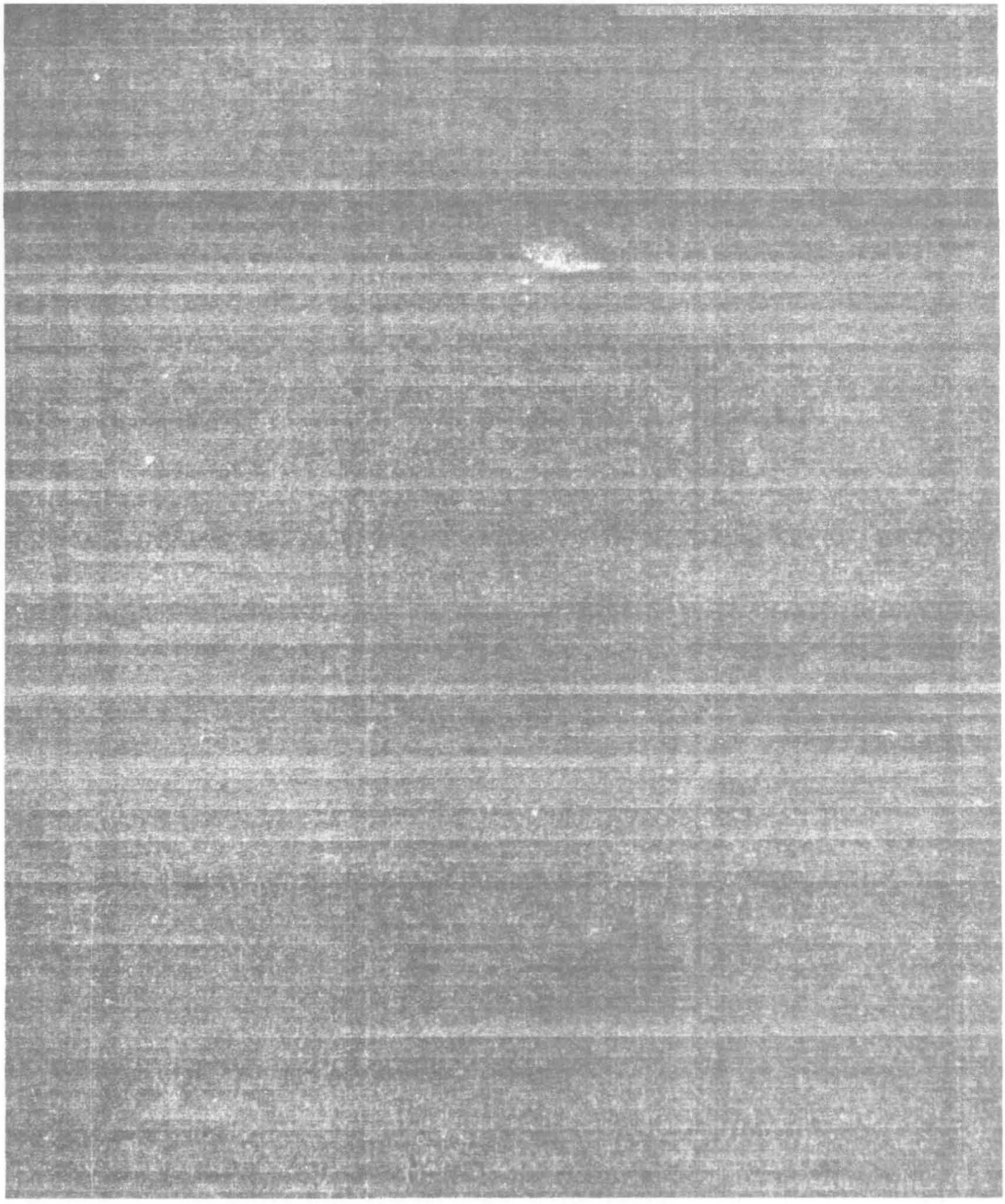

FIGURE 22 CHANNEL 3 UNSQUARED DATA, LINEAR GREY SCALE DISTRIBUTION

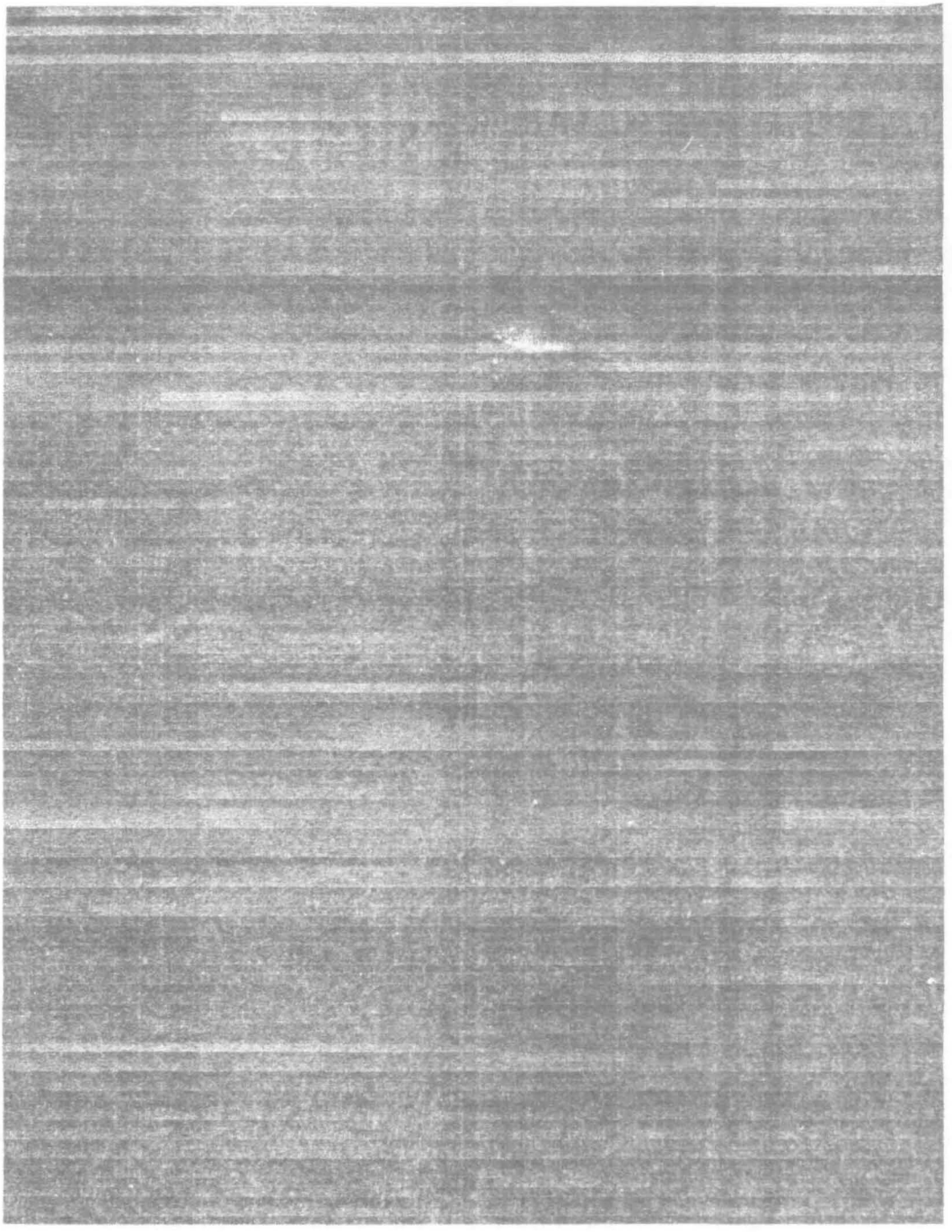

FIGURE 23 CHANNEL 4 UNSQUARED DATA, LINEAR GREY SCALE DISTRIBUTION

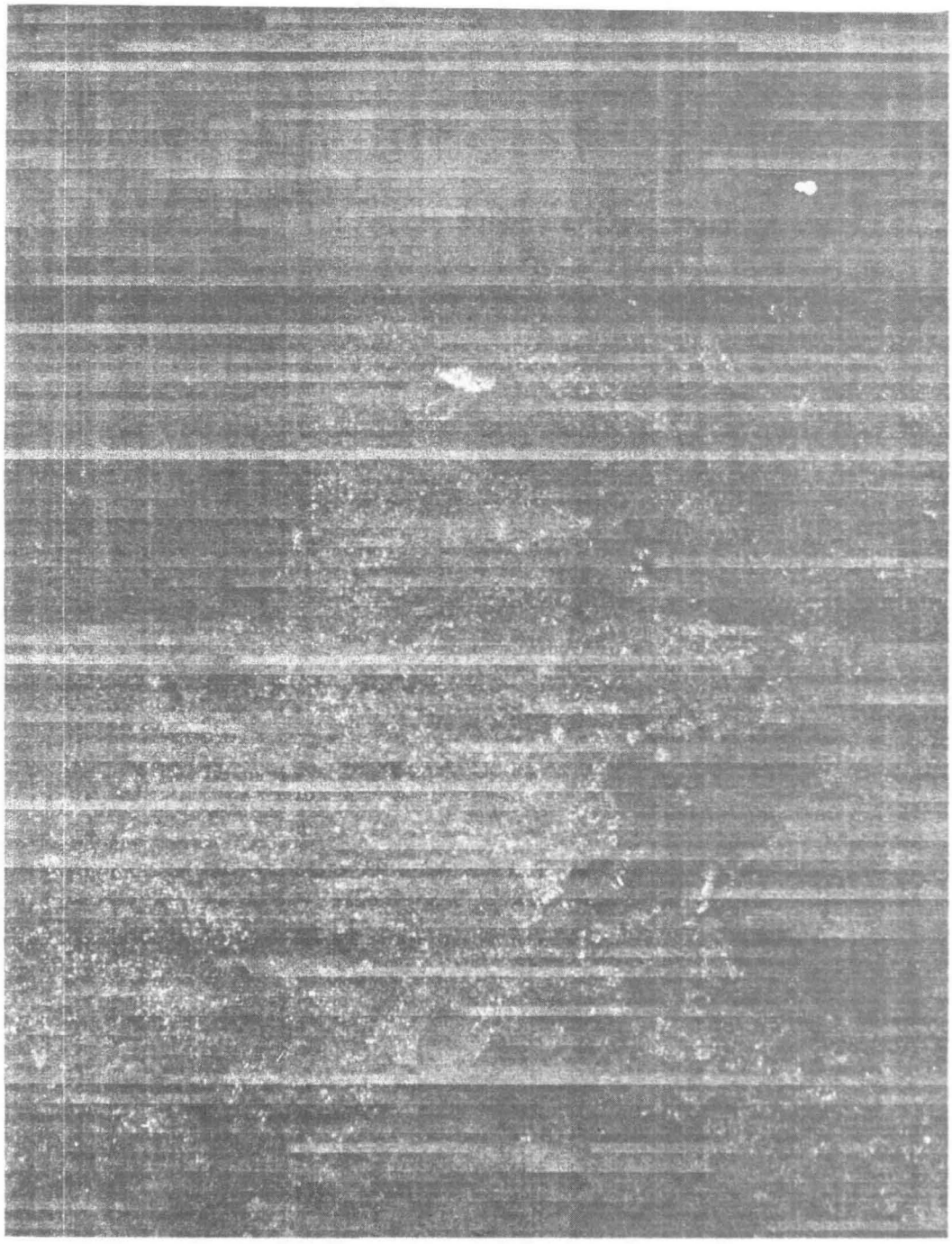

1514131211 10 9 8 7 6 5 4 3 2 1 0
15 22 27 32 35 39 42 45 48 53 55 58 60 62255
IPL 428 FILE 2 FLIGHT 3-13-77 PASS 3 X-BAND HV ICEBERG 2306X1630 1.5M/PIX SQRT 1

FIGURE 24 CHANNEL 1 SQUARED DATA, LINEAR GREY SCALE DISTRIBUTION

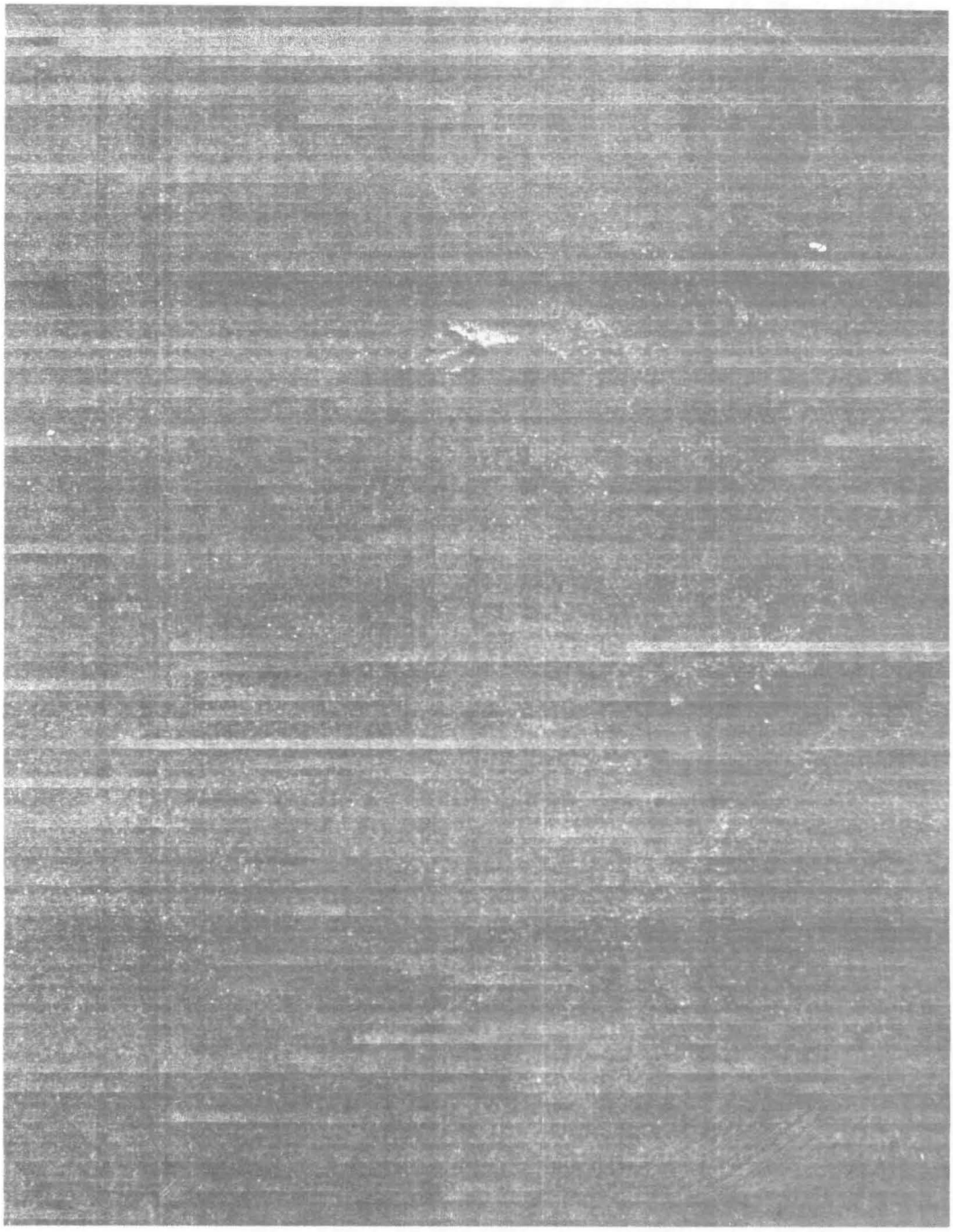

FIGURE 25 CHANNEL 2 SQUARED DATA, LINEAR GREY SCALE DISTRIBUTION

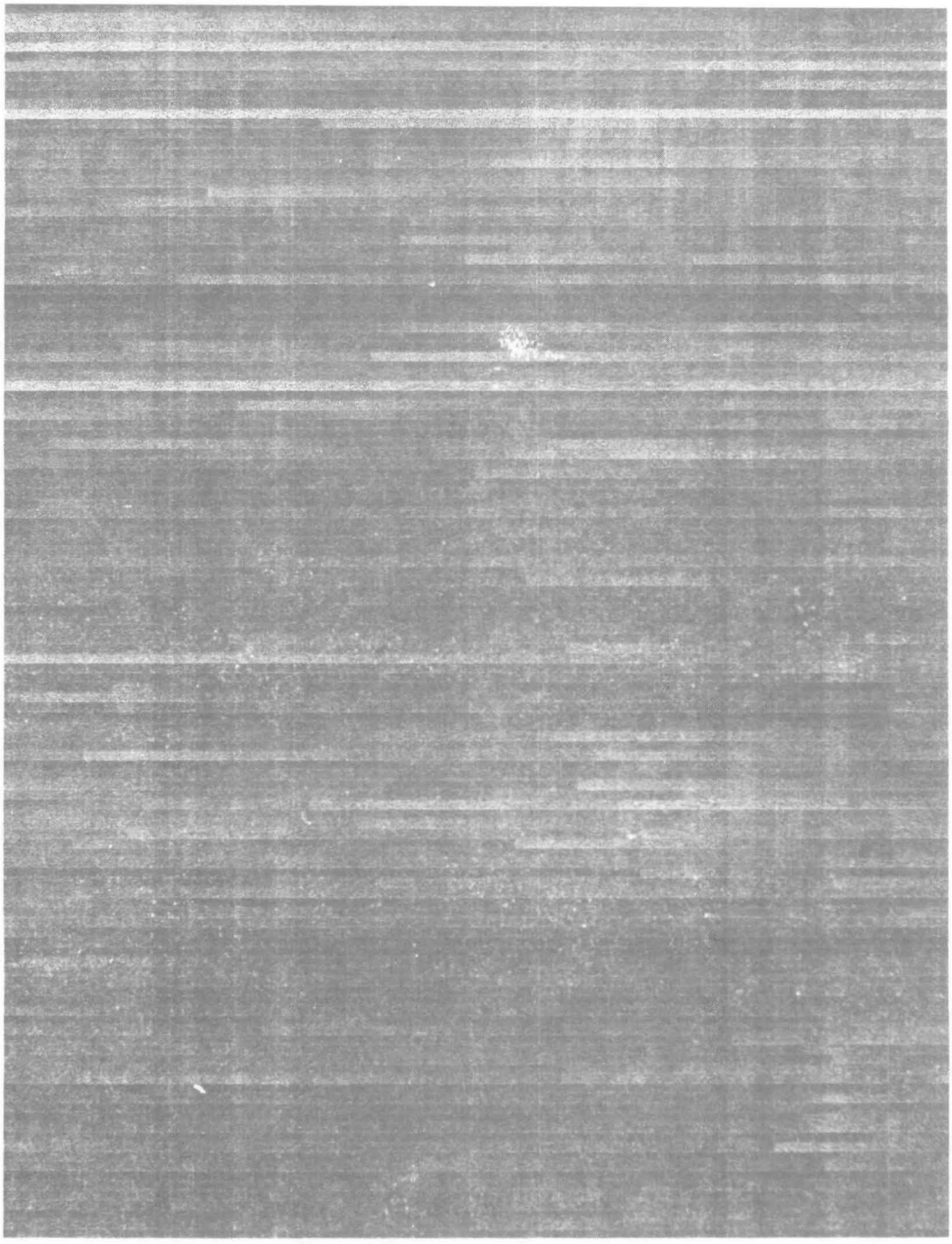

FIGURE 26 CHANNEL 3 SQUARED DATA, LINEAR GREY SCALE DISTRIBUTION

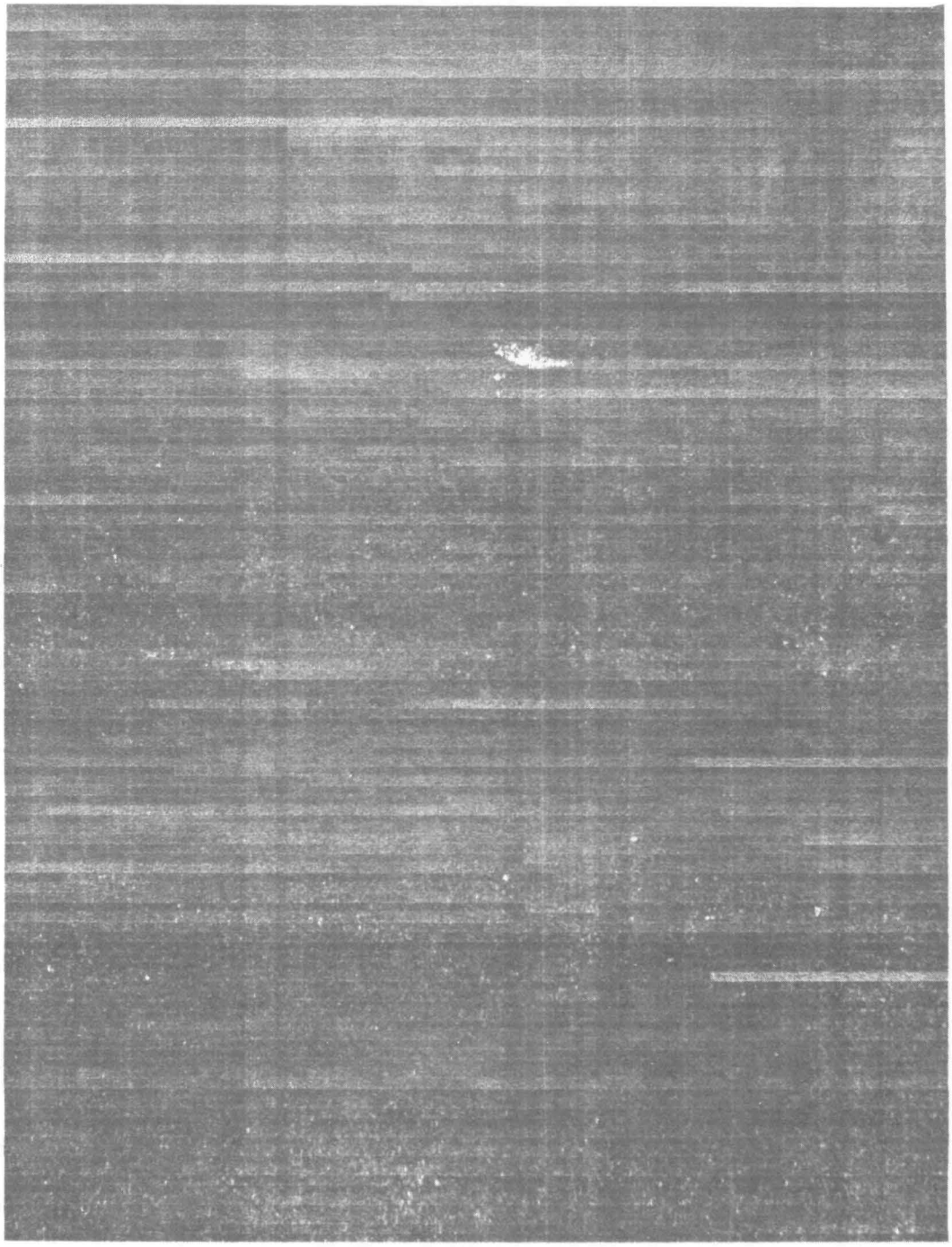

1514131211110 9 8 7 6 5 4 3 2 1 0
30 38 44 50 55 60 64 68 72 75 79 82 88 91255
4 1 2048 1 1530 1
IPL 414 FILE 2 FLIGHT 3-13-77 PASS 3 L-BAND HH ICEBERG 2306X1630 1.5M/PIX SQRT 9

FIGURE 27 CHANNEL 4 SQUARED DATA, LINEAR GREY SCALE DISTRIBUTION

151413121110 9 8 7 6 5 4 3 2 1 0
9 11 13 14 15 16 17 18 19 20 21 22 24 26 28255
1 1 2048 1 1530 1
IPL 428 FILE 2 FLIGHT 3-13-77 PASS 3 X-BAND HV ICEBERG 2306X1630 1.5MPIX SQRT 1

FIGURE 28 CHANNEL 1 UNSQUARED DATA, NONLINEAR GREY SCALE DISTRIBUTION

FIGURE 29 CHANNEL 2 UNSQUARED DATA, NONLINEAR GREY SCALE DISTRIBUTION

151413121110 9 8 7 6 5 4 3 2 1 0
13 15 16 17 18 19 20 21 22 23 24 25 26 28 30255
3 1 2048 1 1530 1
IPL 414 FILE 1 FLIGHT 3-13-77 PASS 3 L-BAND HV ICEBERG 2306X1630 1.5M/PIX SQRT 9

FIGURE 30 CHANNEL 3 UNSQUARED DATA, NONLINEAR GREY SCALE DISTRIBUTION

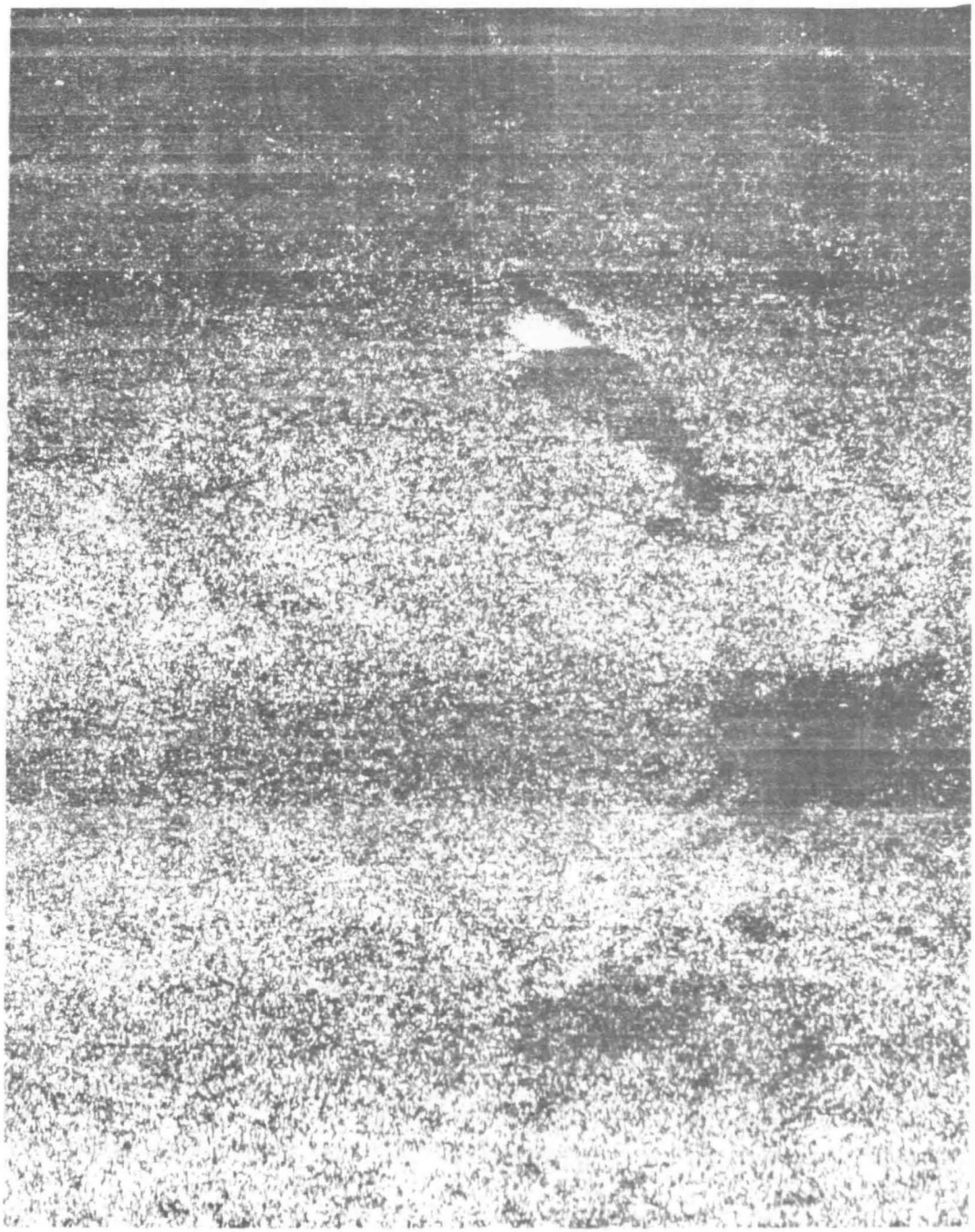

FIGURE 31 CHANNEL 4 UNSQUARED DATA, NONLINEAR GREY SCALE DISTRIBUTION

FIGURE 32 CHANNEL 1 SQUARED DATA, NONLINEAR GREY SCALE DISTRIBUTION

FIGURE 33 CHANNEL 2 SQUARED DATA, NONLINEAR GREY SCALE DISTRIBUTION

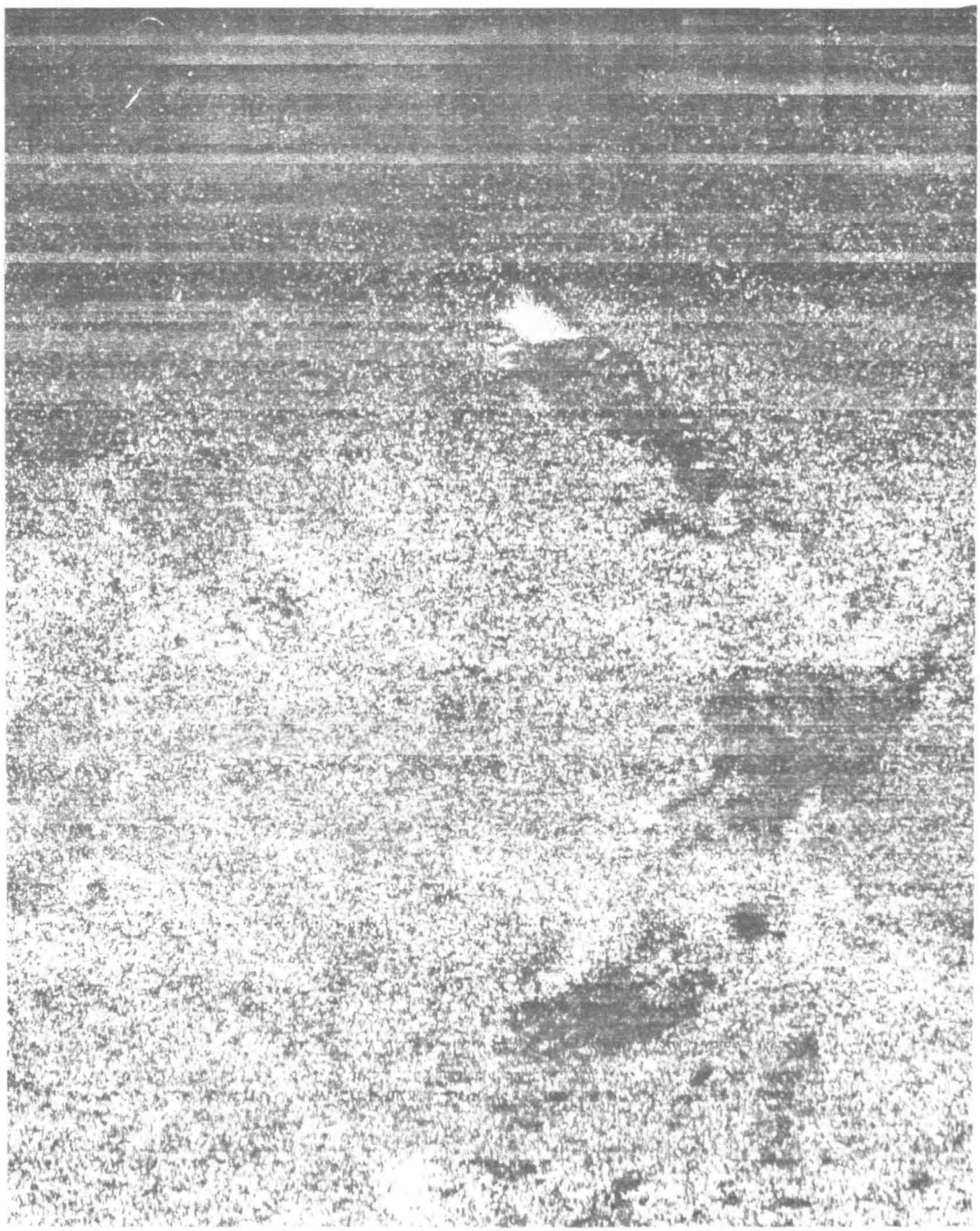

FIGURE 34 CHANNEL 3 SQUARED DATA, NONLINEAR GREY SCALE DISTRIBUTION

FIGURE 35 CHANNEL 4 SQUARED DATA, NONLINEAR GREY SCALE DISTRIBUTION

As the unequal and equal interval quantizations are based only on the combined histograms of the pack ice areas, these regions will be more enhanced than others. This enhancement of the pack ice regions is more evident in the unequal interval quantized images than with those with equal interval quantization. It is difficult to assess the quality of the imagery that can be obtained by considering the combined histogram of the whole image and using unequal interval quantization.

From the shape of the histogram obtained, it is clear that most of the data points or intensity values for each region are confined over a narrow band of values. This is especially true for the X-band channels where the distribution produces a narrow peak as compared to that of L-band channels. The task is to sub-divide this narrow band of values and assign appropriate grey-tone levels based on equal density quantization so that contrast between features is enhanced.

3.2.6 Signal to Noise Ratios. The signal or clutter to noise ratios were computed by using the mean values for different regions presented in Table 1. The noise level corresponded to the mean value obtained for the shadow region. The clutter to noise ratio in dB obtained for the various regions are given in Table III while the iceberg to clutter ratios are provided in Table IV. It should be pointed out that these values are not normalized either for the angular variations or the antenna pattern effects. However, these values provide some measure of quantitative contrast among various regions.

The X-band channels in general provide a higher ratio than L-band channels, the difference being as much as 6 dB in the case of iceberg. The ratios for the Pack Ice Type 3 regions were computed by averaging over the five areas shown in Figure 10. The clutter to noise ratios for some "open water" areas is negative and for X-HH it is -5.466 dB. The minimum contrast ratio distinguishable by the human eye has been found to be 1.5 dB (Larson et al, 1978). The contrast ratio is defined as the ratio of clutter plus noise and noise alone. As a result, the minimum clutter to noise ratio which is detectable is -3.9 dB, which implies that contrast of a clutter level below the noise level is detectable.

The values presented in Table III and IV are as much as 5 dB lower than those presented by Larson et al, (1978) based on the same data. This discrepancy can be attributed to the problem of accurately locating and identifying shadow and iceberg regions on the radar image and corresponding magnetic tape. The nature of the problem is illustrated by the grey-tone representation of the shadow region in expanded scale as shown in Figure 36. Each pixel is reproduced 5 times producing an enlarged image of the

shadow and iceberg region. As seen from these images, it is difficult to delineate the boundary between the iceberg and the shadow with a great degree of accuracy especially for the L-band channels. A different selection of regions for averaging will produce different mean intensity values for the shadow and iceberg, thus introducing discrepancy in the obtained results. In computing means for the iceberg and shadow regions, care was taken to disregard points at the boundaries. These values were used to produce Tables III and IV. However, if more points are disregarded at the boundaries, averaging is taken over concentrated regions, different values are obtained as shown in Tables V and VI. Thus, Tables III and IV probably represent the worst case and Table V and VI the best. The increase in the clutter and noise ratio for the two cases is as much 9 dB for the iceberg.

TABLE III CLUTTER TO NOISE RATIO (dB)

Ice Type	Channel 1 X-Band-HV	Channel 2 X-Band-HH	Channel 3 L-Band-HV	Channel 4 L-Band-HH
Iceberg	16.280	12.801	10.108	10.658
First Open Water	2.264	-0.016	-0.022	-0.767
Second Open Water	3.560	-0.632	-2.117	-4.108
Third Open Water	-0.265	-5.466	-1.710	-0.741
Pack Ice - Type 1	6.271	4.077	1.636	2.981
- Type 2	8.546	4.650	0.129	-2.035
- Type 3 (Avg.)	9.413	4.457	1.413	2.456

TABLE IV ICEBERG TO CLUTTER RATIO (dB)

Ice Type	Channel 1 X-Band-HV	Channel 2 X-Band-HH	Channel 3 L-Band-HV	Channel 4 L-Band-HH
First Open Water	14.016	14.405	12.356	11.424
Second Open Water	12.720	13.433	12.225	14.766
Third Open Water	16.546	18.267	11.818	11.399
Pack Ice - Type 1	10.010	8.724	8.472	7.677
- Type 2	7.734	8.151	9.979	12.692
- Type 3 (Avg.)	6.868	1.354	8.696	8.215

* Shadow region of data used to represent Noise.

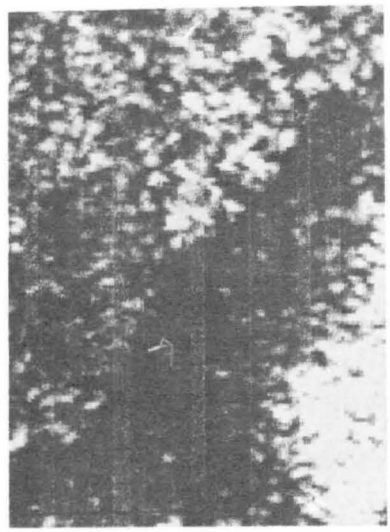

X-HV

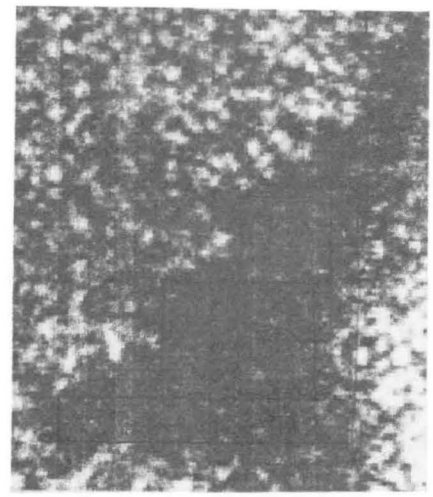

X-HH

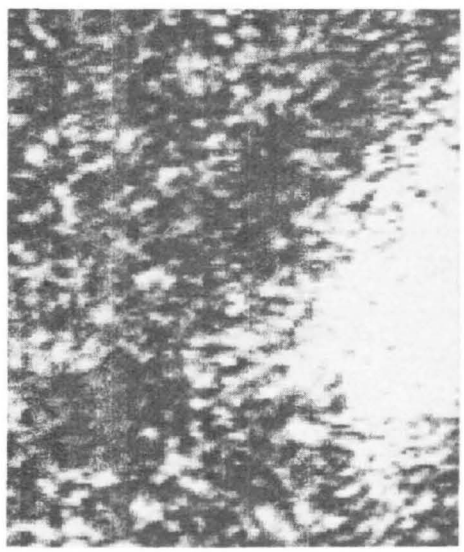

L-HV

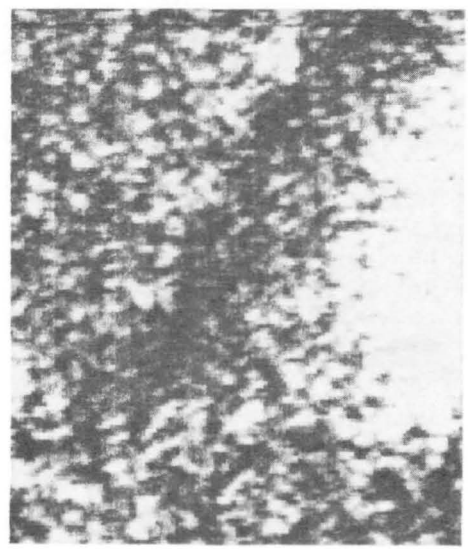

L-HH

FIGURE 36 SHADOW AREAS OF FOUR CHANNELS

TABLE V CLUTTER TO NOISE RATIO (dB), CONCENTRATED REGIONS

Classification	Channel 1 X-HV	Channel 2 X-HH	Channel 3 L-HV	Channel 4 L-HH
Iceberg	21.352	18.351	15.516	16.600
First Open Water	3.696	-0.854	1.336	3.331
Second Open Water	4.992	0.118	1.467	-0.010
Third Open Water	1.166	-4.716	1.874	3.356
Pack Ice - Type 1	7.702	7.702	5.220	7.079
- Type 2	9.978	9.978	3.714	2.063
- Type 3 (Avg.)	10.844	10.844	4.997	6.540

TABLE VI ICEBERG TO CLUTTER RATIO (dB), CONCENTRATED REGIONS

Classification	Channel 1 X-HV	Channel 2 X-HH	Channel 3 L-HV	Channel 4 L-HH
First Open Water	17.656	19.205	14.180	13.269
Second Open Water	16.360	18.233	14.049	16.610
Third Open Water	20.186	23.067	13.642	13.244
Pack Ice - Type 1	13.650	13.524	10.296	9.521
- Type 2	11.374	12.951	11.802	14.537
- Type 3 (Avg.)	10.508	13.144	10.519	10.060

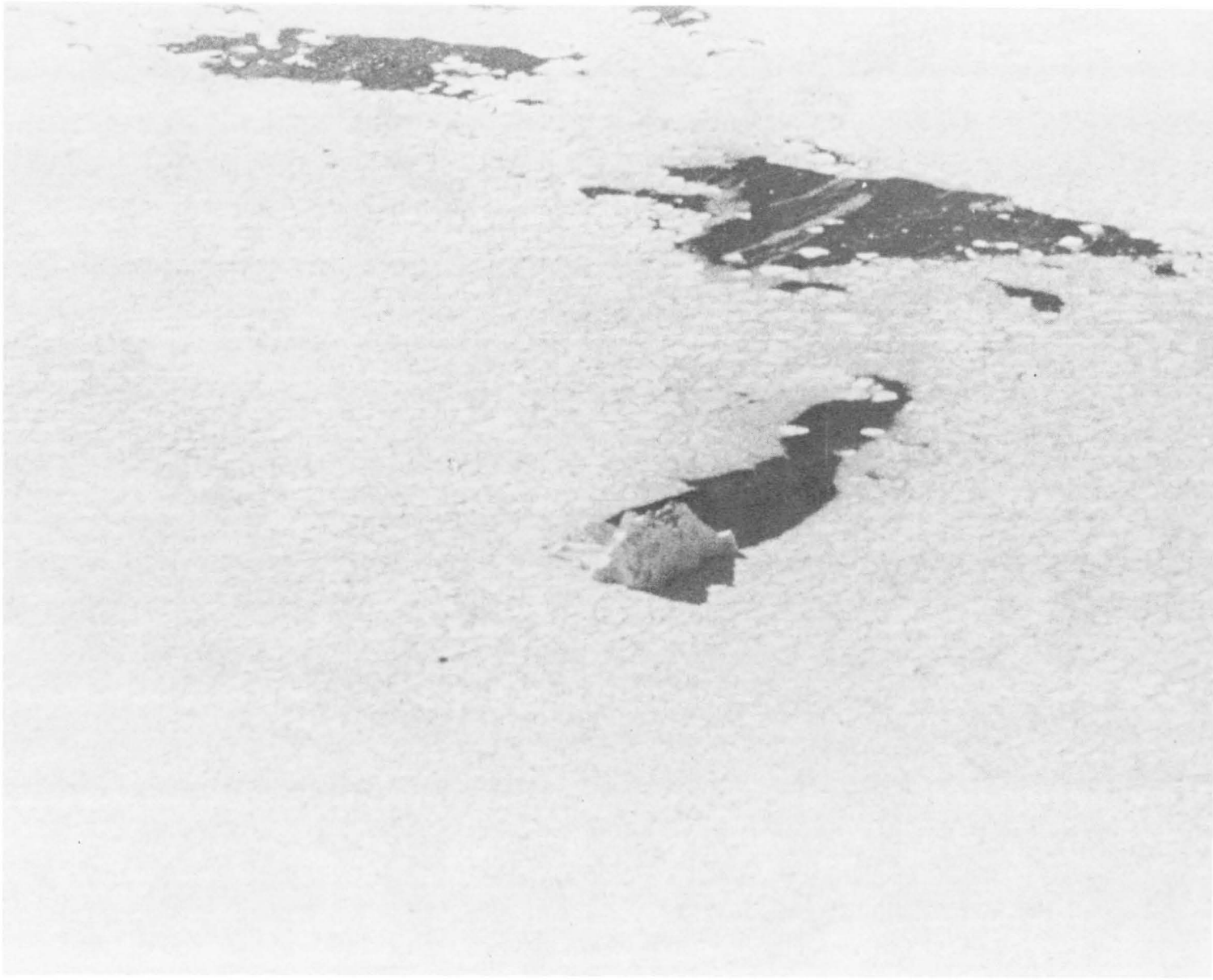

FIGURE 37 VISUAL PHOTOGRAPH OF ICEBERG STUDY AREA

4 DISCUSSION

The obtained results presented earlier are discussed in this section for their relevance and application to improving the likelihood of detecting oil pollution in the ice environment, through SAR and reduction of the false alarm risk. From the very limited information which is available, it appears that ice conditions in the Labrador Sea are very dynamic due to the prevailing atmospheric conditions and southward flowing strong Labrador current. As a result, large ice floes are repeatedly formed, broken up into small cakes of about 2-9 m diameter, and subsequently reconsolidated into large floes. The potential fate of the oil spilled under such conditions as a result of the blow-out at the oil well is discussed by LeDrew and Gustajtis (1978). From the available SAR data it appears that combined imagery from the L-band and the X-band channels provides more information than single channel alone. The intensity for each ice region is confined to a narrow band, with distribution being narrower for the X-band than L-band. As has been discussed by other investigators, dynamic range of radar signals from the ice environment is about 30 to 35 dB. However, only part of this range, (about 24 dB) can be accommodated on the photographic film. As a result, it is desirable to have available grey-tone levels digitized from the image plane of the processor so that as much dynamic range as possible is preserved for subsequent digital image generation.

From the available SAR data and studies conducted in the past it appears that in general the return from open water and new ice areas is confined to the lower part of the dynamic range and return from thicker older ice, for example multi-year ice, is confined to the upper part of the dynamic range. As the computed values of the clutter to noise ratio show, return from "open water" or thin ice areas can be below the noise level. It is in these "open water" and thin ice areas where the presence of oil is likely to be detected initially. The presence of oil on the water surface, in the leads, etc., will dampen the prevailing wind induced capillary waves producing contrast between the polluted and unpolluted region. The detection and degree of contrast are mainly dependent on, prevailing wind speed, temperature, size and orientation of the region. The return from an unpolluted region will be more than from the polluted region. So if the return from the unpolluted region is difficult to distinguish it will even be more difficult to delineate the polluted region. It appears that to increase the likelihood of oil detection in leads and thin ice areas, the gain adjustments when collecting SAR data should be such that the return from open water or thin ice areas falls in the middle of the dynamic range

of the system. This will undoubtedly result in saturated return from thicker ice areas, but it will increase the possibility of detecting oil and reduce the false alarm risk.

The histograms of the digital radar data obtained from the results provide significant information which can be effectively used to enhance significant features of the imaged scene. A simple, inexpensive graphic recorder can be used to produce grey-tone images. The range of intensities of interest can be displayed more effectively using equal density quantization than equal interval quantization. The lower portion of the dynamic range can be enhanced and upper portion suppressed or vice versa. So out of the one imaged scene, different grey-tone images can be produced corresponding to different portions of the available dynamic range.

If swell pattern is present in the imaged scene then processing should be done so that waves are visible in the "open water" areas if these are present. The limited data available shows that when the data are processed to show waves in the ice, the corresponding waves in the open water areas present in the same scene disappear possibly due to the difference in phase velocity of the waves in the open water areas and ice.

REFERENCES

1. Bates, H.F., "Long Period Gravity Waves in Ice Covered Sea: Small Losses", Journal of Geophysical Research, Vol. 80, pp. 22, (1978).

2. Bates, H.F. and L.H. Shapiro, "Long Period Gravity Waves in Ice Covered Sea: No Losses", Journal of Geophysical Research, Vol. 80, 31 pp., (1978).

3. C-CORE, "Investigation of the Use of Microwave Systems - Detecting and Monitoring Oil Slicks over Ice and Ice Infested Waters", C-CORE Publication No. 78-18, St. John's, Newfoundland. (1978).

4. Dawe, B.R. and S.K. Parashar, "SAR Imaging of Waves on Ice", C-CORE Publication No. 78-8, St. John's, Newfoundland, 14 pp., (July 1978).

5. Elachi, C. and W.E. Brown, Jr., "Models of Radar Imagery of the Ocean Surface Waves, IEEE Transactions on Antennas and Propagation", Vol AP-25, No.1, pp. 84-94, (January 1977).

6. Larson, R., C. Liskow, R. Rawson, R. Shuchman, and R. Smith, "Areas Imaged During Project SAR '77 using the ERIM Four Channel Radar". Project SAR '77 Field Data Report E1, pp., 59, C-CORE Publication No. 77-30, (June 1977).

7. LeDrew, B.R. and K.A. Gustajtis, editors, "An Oil Spill Scenario for the Labrador Sea", C-CORE Publication No. 78-2, St. John's, Newfoundland, pp., 796, (March 1978).

8. Moore, R.K., "SLAR Image Interpretability - Trade-Offs Between Picture Element Dimensions and Non-Coherent Averaging", University of Kansas, Center for Research Inc., Remote Sensing Laboratory, RSL Technical Report 287-2, pp., 44, (January 1976).

9. Parashar, S.K., "Investigation of Radar Discrimination of Sea Ice", (Ph. D Dissertation), University of Kansas, Center for Research Inc., CRES Technical Report 185-13, (1974).

10. Parashar, S.K., B.R. Dawe, and R.D. Worsfold, "Investigation of the Use of Microwave Systems - Detecting and Monitoring Oil Slicks Over Ice and Ice-Infested Waters", C-CORE Publication No. 78-18, St. John's, Newfoundland, (1978).

11. Parashar, S.K, B.R. Dawe, and R.D. Worsfold, "Detection and Monitoring of Oil Pollution in the Ice Environment through Microwave Techniques", C-CORE Publication No. 78-12, St. John's, Newfoundland, 19 pp., August, (1978). Proceedings 5th Canadian Symposium on Remote Sensing, Victoria, B.C., (October 1978a).

12. Parashar, S.K., C. Roche, D. Strong, and R.D. Worsfold, "Preliminary Investigation of Sea Ice SAR Data Recorded Over Hopedale, Labrador, During Project SAR '77", C-CORE Publication No. 78-14, St. John's, Newfoundland, 16 pp., October, (1977). Proceedings 5th Canadian Symposium on Remote Sensing, Victoria, B.C., (October 1978b).

13. Raney, R.K. and R.T. Lowry, "Ocean Wave Imagery and Wave Spectra Distortions by Synthetic Aperture Radar", Proc. Twelfth International Symp. on Remote Sensing of Environment, Manila, Phillipines, (April 20-26 1978).

14. Rawson, R., A. Liskow, A. Kloster, and R. Hamilton, "Final Report, Digitizing of SAR '77 Image Data", Environmental Research Institute of Michigan, Ann Arbor, Michigan, pp., 68, (October 1978).

15. Shuchman, R.A., R.F. Rawson, and E.S. Kasischke, "Analysis of Synthetic Aperture Radar Ocean Wave Data Collected to Marineland and Georges Bank", Final Report to NOAA on Contract 04-6-158-44078, (April 1977).

16. Winsor, W.D. and B.R. LeDrew, "Ice Feature Characterization - Labrador Offshore", Field Data Report E14, C-CORE Publication No. 78-4, St. John's, Newfoundland, pp., 58, (May 1978).

17. Worsfold, R.D., D. Strong, and W. Wedler, "Project SAR '77", Fourth International Conference on Port and Ocean Engineering Under Arctic Conditions, September 26 - 30, 1977, Memorial University of Newfoundland, St. John's, Newfoundland, (1977).